Czech University of Life Sciences Prague
Faculty of Environmental Sciences

Department of Water Resources and Environmental modelling
Environmental Modelling Program

Mathematical and experimental modelling of transport of ash in watershed

Master thesis of:
Leyre Tanco Allocchio

Supervisor:
doc. Ing. Michal Kuráž, Ph.D.

30.03.2023

CZECH UNIVERSITY OF LIFE SCIENCES PRAGUE

Faculty of Environmental Sciences

DIPLOMA THESIS ASSIGNMENT

Bachelor of Science Leyre Tanco Allocchio, BS

Environmental Modelling

Thesis title

Mathematical and experimental modeling of transport of ash in watershed

---

Objectives of thesis

Conduct laboratory experiments with artificial rain simulator, post-process experimental data, and calibrate mathematical model.

Methodology

0. literature retrieval
1. artificial rain simulator
2. continual surface runoff sampling
3. data postprocessing – assembling concentration outflow curves
4. objective function definition
5. inverse modeling

The proposed extent of the thesis

50-60 pages

Keywords

forest fires, forest fire residuals, kinematic wave, trnasport processes, inverse modeling

---

Recommended information sources

Hugh G. Smith, Gary J. Sheridan, Patrick N.J. Lane, Petter Nyman, Shane Haydon: Wildfire effects on water quality in forest catchments: A review with implications for water supply, Journal of Hydrology 396 (2011) 170–192

M. Kuraz, J. R. Bloecher: Hydrodynamics in porous media

R. Smith, D. Goodrich, D. Woolhiser, and C. Unkrich. Kineros2: A kinematic runoff and erosion model, 01 2000. https://www.tucson.ars.ag.gov/kineros/.

The Diploma Thesis Supervisor

doc. Ing. Michal Kuráž, Ph.D.

Supervising department

Department of Water Resources and Environmental Modeling

Advisor of thesis

Johanna R. Blöcher

Electronic approval: 15. 11. 2021

prof. Ing. Martin Hanel, Ph.D.

Head of department

Electronic approval: 24. 11. 2021

prof. RNDr. Vladimír Bejček, CSc.

Dean

Author's Statement

I hereby declare that I have independently elaborated the diploma/final thesis with the topic of: **Mathematical and experimental modelling of transport of ash in watershed** and that I have cited all the information sources that I used in the thesis and that are also listed at the end of the thesis in the list of used information sources.

I am aware that my diploma/final thesis is subject to Act No. 121/2000 Coll., on copyright, on rights related to copyright and on amendment of some acts, as amended by later regulations, particularly the provisions of Section 35(3) of the act on the use of the thesis.

I am aware that by submitting the diploma/final thesis I agree with its publication under Act No. 111/1998 Coll., on universities and on the change and amendments of some acts, as amended, regardless of the result of its defence.

With my own signature, I also declare that the electronic version is identical to the printed version and the data stated in the thesis has been processed in relation to the GDPR.

Leyre Tanco Allocchio

Acknowledgement

I would like to thank my supervisor, doc. Ing. Michal Kuráz and, her office colleague Johanna R. Blöcher for their patience and help throughout this project.

Leyre Tanco Allocchio

Abstract

In a context of global change, in which human practices catalyse a change in land use that promotes erosion, loss of biodiversity and pollution, this work will study in a laboratory the possible flow of ash after a wildfire to determine the impact of this ash load on water quality. In order to simulate the rainfall-runoff processes accurately in a catchment, it is essential to calibrate our hydrological model properly. Using the inverse analysis of the governing flow equation of motion, we focus to solve the non-linear differential equations with inverse modelling of a hydraulic laboratory experiment. A well-calibrated hydraulic-hydrologic model can give us a deep insight into the different hydrologic processes and, consequently, improve water management and pollution prediction risk assessment in diverse areas. The results obtained show the parameterization of the advective component of the ash flow equation. In this contribution the aim is to establish an approach to this issue to continue in this line of research and to discern in future studies which populations are susceptible to this critical event, whose threat is becoming increasingly likely. The ultimate goal is to support gubernamentals decision-makers to prevent or be more prepare to future threats.

Contents

List of Symbols

α	Coefficient in relationship between runoff rate and storage per unit area
λ	Determines how size of the step in the Gradicent Descent method
β	Intensive property; values are independent of the amount of mass present
γ	Boussinesq coefficient
ρ	Density of fluid $[ML^{-1}]$
$\forall$	Volume element $[L^3]$
A	Cross-sectional area $[L^2]$
a	Acceleration $[LT^{-2}]$
$d\vec{A}$	Area normal vector
B	Extensive property; values depend on amount of mass present
bw	Bottom width $[L]$
C	Depth-averaged solute concentration $[M/L]$
D	Dispersion coefficient
c	Chezy friction coefficient $[L^{1/2}T^{-1}]$
F	Force $[MLT^{-2}]$
g	Gravity acceleration $[LT^{-2}]$
h	Water surface elevation or depth of surface runoff $[L]$
M	Mass [M]
m	Cross-sectional area in prismatic channel $[L^2]$
n	Manning's roughness coefficient $T/[L^{1/3}]$
Q	Discharge $[L^3T^{-1}]$

Q_{in}	Inlet flow $[L^3T^{-1}]$
Q_{out}	Outlet flow $[L^3T^{-1}]$
q	Discharge per unit width (can be either flow in a channel or lateral inflow $[L^2T^{-1}]$
R	Hydraulic radius [L]
r	Rainfall rate $[LT^{-1}]$
S	Storage $[L^3]$
S_o	Bottom channel slope $-\partial z/\partial x$
S_e	Eddy losses slope
S_f	friction slope
t	Time [T]
$\vec{u}$	Velocity of fluid vector
u_x	Velocity of fluid on x direction $[LT^{-1}]$
W_f	Wind shear factor
x, y, z	Cartesian coordinates

List of Figures

List of Acronyms

WHO World Health Organization 1

WMO World Meteorological Organization 6

DEoptim Differential Evolution Optimization Algorithm 15

DE Differential Evolution 67

INE National Institute of Statistics in Spain 5

EEA European Environment Agency 4

GISS NASA's Goddard Institute for Space Studies 3

LMA Levenberg-Marquardt algorithm 15

NR Newton-Rapshon method 60

GD Gradient Descendent method 60

RS Rainfall Simulator 17

CHAPTER 1

Literature Review

1.1 Water as a resource

Water is a vital necessity and an universal right. The right of water was established in 1976 by the United Nations' International Covenant on Economic, Social and Cultural Rights, as an implicit part of the right to an adequate standard of living and the right to the highest attainable standard of physical and mental health. Later, on 28 July 2010, the United Nations General Assembly explicitly recognised the human right to water and sanitation, reaffirming that clean drinking water and sanitation are essential for the realisation of all human rights.

"Everyone has the right to the continuous availability of sufficient, healthy, physically accessible, affordable and acceptable quality water for personal and domestic uses".

That means that for fulfilled this right water must be, a quantity between 50-100 L/daily per person, have quality standards and guidelines of *World Health Organization* (WHO) must be followed, be found at less than 1000 m distance from the household, and the cost should not exceed 3% of

household income.

Despite this basic right, which is a key measure for the development of a dignified life, according to World Health Organization in 2022 there are at least 2 billion people in the world use a drinking water source that is microbiologically (faecally) contaminated, causing an estimated 485 000 diarrhoeal deaths each year. Additionally, an increasing number of countries are reaching alarming levels of water scarcity and 1.4 billion people live in areas with sinking ground water levels (Mouël and Forslund, 2017) but the situation worsens over time, because it increases by more than 2 billion people out of the world's 7.8 billion in the world living in countries with water scarcity and experience severe water scarcity for at least one month per year, a situation that will likely continue in some regions because of climate change and population growth (UNICEF et al., 2022). In 2020 74% of the world's population used safely managed drinking water, up from 62% in 2000 (UNICEF et al., 2022), although the continuous enhance, these numbers that are concentrated in the most disadvantaged areas of the world must continue to decrease, every one of these preventable deaths is a tragedy . The knowledge and technologies exist to be able to solve this situation in which many people in poor countries are suffering, knowledge of water collection, supply, treatment, and disinfection of water. Sanitation infrastructures must be prepared to be able to supply a quality quantity of water to households, while avoiding sources of pollution of water resources, both point sources of anthropogenic or natural origin and diffuse sources, mostly from agriculture (Bartram et al., 2002).

According to the United Nations, 68% of the global population is expected to live in large urban areas by 2050. This poses a significant challenge for urban planners and decision-makers whose ultimate objective is to keep citizens' optimal living conditions. The projected increases in population and income, combined with changes in consumption patterns, result in increased demand for food, feed, and water in 2050, so there is a necessity to covers this demands in good terms.

Despite the current situation of this 2 billion people, without wishing to belittle them, water is threatened by anthropogenic factors such as pollution or natural factors such as drought or contamination after a fire. This paper will deal with the second type of threat related to natural hazards.

1.2 Natural hazard influenced by climate change

Natural hazard represents the possibility in probabilistic terms that a territory will undergo modifications as a consequence of natural processes, causing negative natural, economic, material or human damage. In the context of climate change impacts, risks result from dynamic interactions between climate-related hazards with the exposure and vulnerability of the affected human or ecological system (Pörtner et al., 2022). The consequences of climate change around the world increasingly affect marine, terrestrial and freshwater ecosystems and ecosystem services, water and food security, settlements and infrastructure, health and economies, especially through stresses and compound events, and may even increase the likelihood of conflict where Africa was found very vulnerable (Cappelli et al., 2022).

According to an ongoing temperature analysis led by scientists at *NASA's Goddard Institute for Space Studies* (GISS), the average global temperature on Earth has increased by at least 1.1° Celsius since 1880. Most of the warming has occurred since 1975, at a rate of roughly 0.15 to 0.20°C per decade. Increases in global mean surface temperature (GMST), relative to pre-industrial levels, affect processes that involve certain risks that are correlated, and they perform a cascade risk such as the following chain of risks: heatwaves, droughts, water scarcity, desertification, land degradation, wildfire damage, soil erosion, vegetation loss, food security, etc (Shukla et al., 2019). Continuing with increasing warming, the frequency, intensity, and duration of heat related events including heatwaves and droughts are projected to continue to raise through the 21st century (Shukla et al.,

2019).

In Europe in 2002 there was already a shortage of water, that supposed may be the most urgent health problem at that time facing some European countries, exacerbated by geography, geology and hydrology (Bartram et al., 2002). Water scarcity is a growing problem, precipitation changes that accompany climate change will exacerbate water storages in some parts of the world while increasing water availability in other areas (Nelson et al., 2010). In fact, in Europe suffered during summer 2022 there was the most severe drought in Europe in 500 years (J et al., 2022).

Drought is a phenomenon that influences limiting capacity for renewable water availability surface water and groundwater. In Europe, water resources are unevenly distributed between and within countries (Bartram et al., 2002), which can be extrapolated to different parts of the world. This can be seen in Europe, according to an *European Environment Agency* (EEA) 2020 publication, annual precipitation trends indicate that the north has become between 10% and 40% wetter over the last century, while the south has become up to 20% drier. Likewise, frequency and intensity of droughts are projected to increase particularly in the Mediterranean region and southern Africa (Shukla et al., 2019).

Water scarcity is particularly pronounced in the Near East/North Africa and the South Asia regions and is likely to worsen as a result of climate change in many regions however while supplies are scarce in many areas, there are ample opportunities to increase water use efficiency (Mouël and Forslund, 2017). Drought risks and related social damages are projected to increase with every degree of warming with aridity zones potentially expand by one-quarter of the 1990 area by 2100 and the projected population exposed to extreme-to exceptional low total water storage is up to 7% over the 21st century (Pörtner et al., 2022).

In the 2°C temperature rise scenario, in southern Europe, more than a third of the population is projected to be exposed to water scarcity and the risk is projected to double at 3°C; in North Africa, the western Sahel and

southern Africa, the frequency and duration of meteorological droughts are projected to double over these areas; and in large areas of northern South America, the Mediterranean, western China and the high latitudes of North America and Eurasia, frequency of extreme agricultural droughts is projected to be 150 to 200% more likely at 2°C, and more than 200% more likely at 4°C (Pörtner et al., 2022).

1.3 Wildfire events

1.3.1 Global significance and causes

In response of global warming, regional increases in temperature, aridity and drought have increased the frequency and intensity of fire (McCarthy et al., 2001). The threat of forest fires is a natural catastrophe or hazard that has been closely linked to humans since their inception, although independently of humans they are part of the natural succession of some ecosystems, forests, grasslands and tundra. Wildfire poses an important threat to life, property, infrastructure, and natural resources in fire-prone forest areas (Smith et al., 2011). The main causes are lightning, volcanoes and human action, the latter being the main cause in the Mediterranean basin area, for example, from *National Institute of Statistics in Spain* (INE) is known that in Spain, which represents about 40% of the burned surface of Europe each year, in the decade from 2006 to 2015 there were 52.70% of the fires caused intentionally, which burned an area of almost 60%, and on the other hand, those caused by lightning were not reached 5% in number or 5% of the total burned area; and the rest were due to unknown causes and/or negligence or accidents. The interaction between fire, land use change, particularly deforestation, and climate change, is directly impacting human health, ecosystem functioning, forest structure, food security and the livelihoods of resource-dependent communities (Pörtner et al., 2022).

1.3.2 Frecuency and Severity

Wildfires are a serious problem in many countries, according to the FAO, that represents 13% of the world's total burnt forest area, with 350-400 million hectares of forest burning each year. The trend of these unprecedented fires is occurring not only in Europe, the Middle East and North Africa, but throughout the world such as in California, Australia, South America, etc (J et al., 2022). According to a new *World Meteorological Organization* (WMO) report in 2022, climate change and land-use change are projected to make wildfires more frequent and intense, with a global increase in extreme fires of up to 14% by 2030, 30% by the end of 2050 and 50% by the end of the century. Forest fires ravaging Europe clearly demonstrate the effects of climate change. The climate change is affecting this phenomenon, not only the expansion of affected areas, but also the lengthening of the fire season, extending beyond the traditional summer months and increasing frequency and intensity of forest fires (J et al., 2022). Frequency of wildfires widely varies among vegetations types and climates, is directly related to fuel loads, that were affected for instance in some European regions due to rural depopulation, fire suppression as measure management and introduction of more inflammable tree species as of pines or eucalypt; led to less frequent but more severe wildfires (Williams et al., 2002). Fire severity explains the degree of destruction and depends on the interaction between the duration of the burning, intensity (the rate at which thermal energy is produced), the biomass, soil, terrain and local climate (Shakesby and Doerr, 2006). Therefore, fuel load may be affected the availability of drier fuel.

1.3.3 Distribution of affected regions

Wildfire is an important disturbance factor, it can be important if not the major cause of hydrological and geomorphological change in fire-prone landscapes (Shakesby and Doerr, 2006). In this paper, Shakesby and Doerr

(2006) review the literature over the last century related to the impacts of the fire as an agent on hydrological and geomorphological process. They said that since 80's it began to grow the literature concern this topic in other areas outside the U.S., these are Mediterranean Basin, Australia and South Africa. Since these areas are prone to this threat, in south-eastern Australia during 2019-2020 wildfires resulted in 33 people killed, a further 429 deaths and 3230 hospitalizations due to cardiovascular or respiratory conditions, and $1.95 billion in health costs. In Australia where large areas large areas were affected by droughts from 2002 to 2009 based on Advanced High-Resolution Radiometer (AVHRR) satellite data (Donohue et al., 2009).Hence, backing up this data there are projected in southern and eastern Australia and over most of New Zealand, more droughts and extreme fire weather (Pörtner et al., 2022).

An example of threat in quality of water was after the events occured in southeastern Australia, wildfires have burned forested reservoir catchments which supply potable water to Sydney (2001 wildfire), Canberra (2003), Adelaide (2007), Melbourne (2009), as well as various regional towns (Smith et al., 2011). During last decade large wildfires burned widely forest catchments containing streams and reservoirs utilised for water supply Smith et al. (2011). In particularly, in Canberra there was a disruption to the supply of drinking water after the 2003 wildfire, the constructions of a flocculation and filtration plant to treat with turbidity was needed with a buggedt over 38 million (AUD). Australia is one of the major places that shows the dependency of water quality changes on post-fire rainfall events and the regional diversity of landscape controls influencing post-fire runoff, erosion and downstream constituent flux.(Smith et al., 2011).

Forest fires ravaging Europe clearly demonstrate the effects of climate change. In Europe the Commission's Joint Research Centre (JRC) concludes in its latest edition in 2021 of its Annual Report on Forest Fires in Europe, the Middle East and North Africa, that the burnt area was 550000 ha of land burnt in 2021, more than twice the area of Luxembourg and less than

the highest record of 10000 km² since 2006 (begin of record). However, 2022 proved to be the year with the highest number of fires and the largest area burnt since 2006, with a burnt area of more than 860000 ha in the EU (J et al., 2022), compared to an average of just over 260,000 ha in 2006-2021 (Copernicus, September 2022).

1.4 Post-fire hydro and geomorfological effects in the environment

It has been known since Brown (1972) that wildfires significantly affect changes in the hydro and geomorphology of the affected basin.

1.4.1 Reduction in infiltration

After a wildfire, it is accepted that the infiltration will be comparatively less to unburnt areas, this is caused because the vegetation and litter cover is removed, the transpiration, interception and surface storage capacity for rain their reduce or stops. (Shakesby and Doerr, 2006). Depend on different percentage of vegetation and litter cover rainfall contribution to overland flow, for instance: in locations where there are 60-75% vegetation cover about 2% of rainfall contribute to overland flow, where the cover is 37% about 14% of overland flow and in locations where there is a 10% about 73% of rainfall will become runoff Shakesby and Doerr (2006).

1.4.1.1 Water repellece soil

However, not only the vegetation is causing the increasing in runoff. Since, 1960 it is perceived that fire induced to have a water repellency effect in soils DeBano (2000) and currently it is know much more about the topic. An hydrophobic below or on the soil surface layer can form (Bodí et al., 2011; DeBano et al., 1979; Gabet, 2003). Fire may induce water repellency in a non-repellent soil, and enhance the preexisting repellency

of surface (Shakesby and Doerr, 2006). This depends on the the types of soils and the temperature during burning but also on the amount and type of organic matter consumed during wildfire. DeBano et al. (1979) determined that phenomena of water repellency is due to the mobilization of hydrophobic organic substances that become volatilized in soil a follow a path to release in the atmosphere or following the pression gradient downward until condensation occurs. The less intense the wildfires, the lower the temperatures reached the higher water repellency soil could be presented, Shakesby and Doerr (2006) and DeBano et al. (1979) determine slightly different ranges of temperature classification but between 175-270 ºC they found soils with water repellency could be intensified and over 460-600 ºC destruction water repellency occurs may rise, however the soils after burning results in more friable, less cohesive and more erodible soil.

1.4.1.2 Sealing pores

Another process in the reduction of infiltration could be the sealing of pores by fine soil and ash particles, compactation by raindrop impact, increment the likehood of the occurrence of frozen soil due to the removal of insulating organic matter (Shakesby and Doerr, 2006).

1.4.2 Overland flow Runoff Erosion

After the reduction of infiltration due to the various causes, it causes that erosion to increase Moody and Martin (2001); Smith et al. (2011), there is a clear link between overland flow response and fire severity, finding for example in humid ecosystems great contrasts between pre and post flows fires having an increase in baseflow (Moody et al., 2008). Erosion rate of suspended sediment exports during the first year after the fire will vary between 0.017 and 50 $tha^{-1}yr^{-1}$ over a wide range of basin sizes (0.021-1655 km^2). (Smith et al., 2011). Brown (1972) proved that fires also change the the shape of the flood hydrographs, founding higher flow concentration

peaks or the concentration peaks being more pronounced on the ascending side of the flood hydrograph and, in addition, an increase in the amount of water was observed of runoff. The most likely cause of the sharp peak is Hortonian overland flow enchanced by litter destructions lowering the surface storage capacity of rainfall and reduction surface roughness together with the water repellent nature of the soil (Shakesby and Doerr, 2006). When the ash layer becomes saturated after sufficient rainfall , Santín et al. (2015), runoff carrying capacity has been found enhanced due to increased fluid density by ashes (Smith et al., 2011), reaching surface water bodies.

1.4.3 Quality of water after fires

Impact of wildfire on soil erosion by water induce potential post fire flooding problems and impacts on channel stability as well as implication for water supply (Shakesby and Doerr, 2006). Wildfires can impact in water quality through the increasing levels of nutrients and trace elements, resulting the exceedance of guideline concentration thresholds in reservoirs (Langhans et al., 2016; White et al., 2006). The ash fine sediment is eroded within the first years into the reservoirs (Langhans et al., 2016; Reneau et al., 2007). There is a greater interest in how water quality may be affected after wildfires because post-fire erosion could transport ashes that may become an a source of contamination of water reserves and streams. Researchers present in the previously mentioned most affected geographical areas area; Australia (Lane et al., 2006; Langhans et al., 2016; Santín et al., 2015; Smith et al., 2011; White et al., 2006), Mediterranean (Bodí et al., 2012; Cerdà, 1998) and EEUU (Cole et al., 2020; Ebel et al., 2012; Moody and Martin, 2001; Ryan et al., 2011).

This project is important for decision-making managers, since, for example, they can evaluate the vulnerability of their population and if their water supply comes from a basin where, due to the weather and mythologies, it is known that they are potential to suffer this threat. The administrations

policies should try to anticipate by making good management of their forest resources, adapting water treatment plants and increasing variety of supplies.

CHAPTER 2

Introduction

In a global context of change, there are different hazard risks, some them associated with antropogenic agents but other related with natural factors. Due to the climate change around the world there has been an increase in the number of consequences associated with natural hazard risk. Grow in global mean surface temperature may perform a cascade of risks such as the following chains of risks: heatwaves, droughts, water scarcity, desertification, land degradation, wildfire damage, soil erosion, vegetation loss, food security, etc (Shukla et al., 2019).

In particular, in this work we concern about the problem related with drinking water quality and availability. There exists more than 2 billion out of the world's 7.8 billion people living in countries with water scarcity who have experienced severe water scarcity for at least one month per year (UNICEF et al., 2022). Water scarcity is a growing problem that will exacerbate in some areas all over the world (Nelson et al., 2010), heatwaves and droughts are projected to continue to increase through the 21st century (Shukla et al., 2019). According to EEA 2020 publication, annual precipitation trends indicate that south Europe has become up to 20%

drier over the last century; and in the case of a 2^{o}C rise in temperatures, more than a third of the population is projected to be exposed to water scarcity (Pörtner et al., 2022).
The drought and aridity have increased the frequency and intensity of wildfires (McCarthy et al., 2001). This threat is promoted with not only the expansion of affected areas, but also the lengthening of the fire season, extending beyond the traditional summer months and increasing frequency and intensity of forest fires (J et al., 2022). According to the FAO wildfires represent a 13% of the world's total burnt forest area, with 350-400 million hectares of forest burning each year, becoming a serious problem in many countries. It poses an important threat to life, property, infrastructure and natural resources in fire-prone forest areas (Smith et al., 2011).
Wildfire is an important disturbance agent, it can be important if not the major cause of hydrological and geomorphological change in fire-prone landscapes (Shakesby and Doerr, 2006). Year 2022 proved to be the one with the highest number of fires and the largest area burnt since 2006, with a burnt area of more than 860000 ha in the EU (J et al., 2022).
The role of wildfire as a potent hydrological agent is now widely recognized amongst the scientific, environmental and policy-making communities. (Shakesby and Doerr, 2006). Since the article (Brown (1972)) was published, it is known that wildfires significantly affect changes in the hydro and geomorphology of the affected basin. After a wildfire, it is accepted that the infiltration will be comparatively less to unburnt areas, so the rainfall contributes to create overland flow, runoff and erosion processes (Shakesby and Doerr, 2006).

A series of processes are observed after a wildfire. A reduction in the infiltration increases the erosion rates and this changes the runoff generation which leads to sources of pollutants being delivered to streams and reservoirs, Moody and Martin (2001); Smith et al. (2011). This can potentially result in water supplies not meeting the health guidelines for

consumption Smith et al. (2011); White et al. (2006). Approximately one third of the largest cities in the world (33 cities) obtained a significant proportion of their drinking water from protected forest areas, with a further five cities obtaining water from distant catchment areas which also contained protected forest (Dudley and Stolton, 2003). Furthermore, forest areas are estimated to contribute two-thirds of the freshwater supply in the United States (Smith et al., 2011).
In this study, we focus on how much load of ash may arrive to the drinking water sources, affecting the quality and availability of drinking water to the population. For instance, in Canberra there was a disruption to the supply of drinking water after the 2003 wildfire which was solved by constructing a flocculation and filtration plant to treat turbidity. A 38 million (AUD) budget was needed (Smith et al., 2011).
There is a great interest in how water quality may be affected after wildfires, particularly by researchers located in the most affected geographical areas; Australia (Lane et al., 2006; Langhans et al., 2016; Santín et al., 2015; Smith et al., 2011), Mediterranean (Bodí et al., 2012; Cerdà, 1998) and EEUU (Cole et al., 2020; Ebel et al., 2012; Ryan et al., 2011). An experiment was developed in the laboratory of Faculty of Civil Engineering of the Czech Technical University in Prague (CTU) to determine the flow ash equation - which is the major goal of this project.

2.1 Aims and Goals

This study puts a lot of emphasis in determining or parameterizing flow hydraulic properties and pollutant transport properties. Inverse modelling approach was used because the flow and transport parameters were determined using a mathematical model equation that was solved by a numerical method. During the experiment we collected an observed data over different conditions and with the inverse modelling we obtain the parameter with sufficient acuracy. The same result was obtained under the

simulation of model with DRUtES software (Dual Richards Unsaturated Equation Solver) which works with finite difference method. Objective function (RMSE) was minimized using two iterative different algorithms methods, *Levenberg-Marquardt algorithm* (LMA) and *Differential Evolution Optimization Algorithm* (DEoptim).

CHAPTER 3

Materials and Methodology

In this chapter, the methodology and the data used to model the ash flow in the rainfall simulator experiment are explained. First, the experimental design is in section 3.1. Then the mathematical model framework and its parameters are described in sections, which is physically based because the mathematical models used to describe the components are based on such physical principles as conservation of mass and momentum chapter 4.
Engineers and scientist often need to estimate ruoff rates and volumes from ungaged watersheds. For some purposes, a more precise knowledge is required about the hydrologic response of a watershed. Thus, a model sensitivity to various physical factors or assumptions is needed, and physically based distributed models of runoff are becoming more widely used (Woolhiser et al., 1990).
In this project, the ash flow equation will be obtained by means of an inverse modelling analysis see section 5.3. Inverse modelling refers to an iterative process that seeks to minimise the differences between the observed data set and the expected data set simulated by an existing reference model.
This project is divided into different phases. The first is the collection

of observed or measured data, for which a laboratory experiment was developed (3.1). The second phase is to obtain the simulated data under a theoretical frame of reference (5.2). The third step is the inverse modelling to minimise the deviations between the simulated and observed data (5.3).

3.1 Experimental Design - Experimental Setup

In this study a laboratory experiment was developed with a rainfall simulator device. We are interested in modelling the Overland flow, which is defined as water that flows over the land surface as either diffuse sheet flow (laminar flow) or concentrated flow (turbulent flow) in rills and gullies (Buda, 2013). The appearance of free water on the soil surface, called ponding, gives rise to runoff in the direction of the local slope.
Rainfall can produce ponding by two mechanisms. The first mechanism involves a rate of rainfall which exceeds the infiltration of the soil at the surface, whereas the second mechanism is soil filling, when a soil layer deeper in the soil restricts downward flow and the surface layer fills its available porosity (Semmens et al., 2007). In the first mechanism, the surface soil water pressure head is not more than the depth of water, and decreases with depth, while in the second mechanism, soil water pressure head increases with depth until the restrictive layer is reached, the water-table. This second method is what was done in the laboratory during the experiment, as the fully saturated soil was imposed to (see section. 3.1.3).

3.1.1 Rainfall Simulator (RS)

Rainfall Simulator (RS) have been used as research tools extensively for field and laboratory characterization of hydrogeomorphological studies including runoff, infiltration, and soil-erosion characteristics as well as studies of sediment, nutrient, and pollutant transport within watersheds (Aksoy et al., 2012; Kavka et al., 2019). The primary purpose of a rainfall

simulator is to duplicate the physical characteristics of natural rainfall as closely as possible, simulating natural rainfall accurately and precisely (Aksoy et al., 2012; Kavka et al., 2019).

Desirable characteristics for rainfall simulators, include the rainfall intensity, spatial rainfall uniformity over the entire test plot, the drop size, its distribution, and terminal velocity. Other important characteristics are the accurate control of rainfall intensity; similarity to natural rainfall in terms of kinetic energy; repeatability of applying the same simulated rainstorms; and improved mechanical and technical reliability for simple and easy transportation within research areas (Aksoy et al., 2012; Clarke and Walsh, 2007).

The laboratory *Rainfall Simulator* (RS) equipment that was used in this project is located at the Faculty of Civil Engineering of the Czech Technical University in Prague (CTU) Fig.[3.1].

Fig. 3.1: Rainfall Simulator (RS) in the laboratory of the Faculty of Civil Engineering of the Czech Technical University in Prague (CTU)

Fig. 3.2: Rainfall Simulator (RS) in the laboratory of the Faculty of Civil Engineering of the Czech Technical University in Prague (CTU)

3.1.1.1 Dimensions or Geometry of RS

The dimension of the soil sample or soil container it is 4 m long and 1 m wide, it is a rectangular channel Fig.3.1 and 3.2. The construction permits changes the slope setting between 0 and 40%. There is a generation a wide spectral of rainfall with different intensity, duration, hyetograph and kinetic energy.

3.1.1.2 Characteristics RS

Kavka et al. (2019) specifies the characteristics of the RS, it combines two basic types of nozzles, flat nozzles (VeeJet) with swiping; and full jet nozzles (WSQ) with interruptions. The typical applied rainfall intensity ranged between 20 and 60 mm/h, in our case was set a intensity which is within in usually range operation. But there is a possibility to set a maximal rainfall intensity is 200 mm/h. Water is supplied from the basin in the basement of the hydraulic lab which has a pressure 2–2.5 bar. RS allow to have a control at the manometer on the pump can be regulated with a plug valve on the bypass. The bottom could be freely drained and subdivided into 6 segments.
The *Rainfall Simulator* (RS) and the soil container are equipped with various monitoring sensors and automatic data logging, their automatic monitoring system records surface runoff, soil loss, percolating water, soil water and soil temperature regime (Kavka et al., 2019).

3.1.2 Ash and Soil Sample

The ash sample used was collected by a pine debris incinerator. Since the element used to trace the transport of the ash flow is potassium (K), 3 soil samples were taken and sent in different dislocations to be analyzed, see table 3.1, to know the possible initial concentration at time 0 of potassium in the soil surface.
After the fires on the hillslopes, large reserves of ash can be deposited as in Balmoral wildfire in Sydney 2013 were the ash loads went up to 34 $Mgha^{-1}$ (Santín et al., 2015). Ashe with low-density can be easily dragged by the flow Reneau et al. (2007) which, among others, contain carbon particles, high concentrations of various nutrients and trace elements (Smith et al., 2011). Potassium being a water-soluble element easily translated by the flow.

SURFACE CRUST

Bottle number	Soil [g]	Water [mL]
452	10	800
554	25	800
1	50	800

Tab. 3.1: Soil samples to determine the intial concentration of potassium

3.1.3 Initial and Boundaries conditions

Laboratory conditions allow a perfect control of the system initial and boundaries conditions, and soil surface characteristics, monitoring of the on going processes (runoff, sediment transport, infiltration, rills development etc.) (Kavka et al., 2019). This control system helps to perform various scenarios and replications with different inclination or rainfall characteristics, the main disadvantage of the laboratory conditions could be the disturbed (and translocated) soil sample (Kavka et al., 2019).
The experiment is 1D, it means the flow is observed only in one spatial axis, in this case it corresponds to the flow trajectory, the length of the watershed. The boundary conditions are observed as the rise or elevation in flow along the length of the watershed.

3.1.3.1 Initial conditions

As the initial conditions for all scenarios the soil is fully saturated, pressure head is zero (h = 0). The fully saturated medium is set because we are interested in observing only surface runoff, thus eliminating infiltration or percolation as a factor.

$$\textbf{pressure head} \ = h(x,0) = h_0(x) = 0$$

For each scenario different values for slope and rainfall intensity (rate of flux) were set. So, the effective rainfall and slope are source variables.

3.1.3.2 Top Boundary conditions

Usually, the upper boundary conditions in 1D when we are interested in the ponded infiltration are determined by the rates of potential evapotranspiration, rainfall or irrigation, and the soil vegetation properties (Van Dam and Feddes, 2000).
However, as we are conducting a 1D experiment, we are not interested in the z-axis (depth of soil). In addition, we look only at the x-axis, which represents in this case the length of the basin, the flow path. In this case we select as top boundary, $x = 0$, the outlet point of our basin, the gauging station where the flow data are collected. So the top boundary condition is:

$$y(0, t) = q_{out}$$

3.1.3.3 Bottom Boundary conditions

At the bottom, various forms of head and flux-based conditions could be used, i.e. deep of watertable, free drainage, etc in the z-axis. In the field experiments conditions, with deep water table levels, initial soil moisture condition is determined by the pressure head as a function of soil depth with linear interpolation between depths (Kroes et al., 2017).
In our experiment the bottom boundary conditions corresponds to the highest point of the catchment area, $x = 4$, where at any time we are not going to have any elevation of the flux. So our bottom boundary condition is:

$$y(4, t) = 0$$

3.1.4 Data Collection

Two types of experiments were carried out on the same day, in the CTU laboratory. This first type of experiment has the finality to observe the movement of ash over time, under different initial conditions, rainfall

intensity and slope. The second type of experiment, on the other hand, the aim was to observe the type of hydrological conditions in the catchment, how the water flow behaves in this catchment characterised by this slope, intensity and soil conditions (texture, bulk density, roughness, porosity, structure, etc.).

3.1.4.1 First Experiment

In particularly, in the first type of experiment, it was observe the change in ash concentration over time in the lateral outflow at x = 0, in the top boundary. For this purpose, a load of ash sample was deposited into the upper quarter of the basin, from x(4) to x(3). Two different scenarios were produced, the same procedure under different initial conditions, rainfall intensity and catchment slope conditions, our variable inputs. The variables set for the scenarios were slope and rainfall intensity. During the simulation, the flow samples were taken at regular time intervals of 1 minute for 35 minutes. In all scenarios the same ash load was always introduced in the upper part of the study catchment.

After each simulation, the remaining ash was removed by removing the 3-4 centimetres of soil surface where the ash could be observed. In the upper part, where the ash sample was located before the simulation, the formation of the superficial ash crust could be observed. After removing the ash from the previous performance, the surface was homogenised with a rake, to try to maintain the same roughness in the soil surface. The soil surface was also wetted with a watering can to ensure the condition of total saturation of the soil.

The samples started at 1 litre and then we increased the size to 2 litres. For potassium determination in the laboratory, it was problematic to have such a large sample size. Therefore, the samples in scenario 2 were transferred to 100 ml buffer sizes, and before doing so, the sample bottles were thoroughly shaken. In the end, data from the first experiment was not analyzed because

Fig. 3.3: Resampling of the concentration ash data)

it was considered sufficient for the development of this thesis the analysis of the second experiment.

3.1.4.2 Second Experiment

In the second type of experiment, in particular, we pursued to determine the water flow characteristics that we have in the basin which is dependent on the slope and rainfall intensity. We want to determine the intrinsic roughness coefficient of this basin, which is based on the type of soil, whether it is more or less repellent (porous, structure,etc.) what is equal

to the conditions of the surface layer of the material. This parameter will determine the type of flow that can develop in this catchment, it is important to know this factor because it explains how much friction force the material exerts on the movement of water and it will provide the advection term in the flow equation.

To determine the advection or convection term in the water flow during the experiment throughout this simulation the rainfall was reproduced at a constant intensity, for four minutes, then the simulator was switched off for the same period of time, so in total the cycle had a duration of 8 minutes. This “cycle” of rainfall-on + rainfall-off is repeated another two times in total. For the second scenario, only the first "cycle" had the duration of 8 minutes, the others instead of 8 minutes minutes have the duration of 6 minutes. These data correspond to the measurement of the cumulative weight, in grammes, of the effluent flow during a performance in a rainfall simulator device.

For the first scenario the slope was set at 6% and 37 mm/hrs, while for the second scenario the slope was set at 8% and an intensity of 47 mm/hrs. The fist scenario has a duration of the simulation of 24 minutes $3 \cdot (4+4)$, while in the second scenario the duration was 26 minutes $(4+4)+(3+3)\cdot 3$. So, the first dataset is longer 1614 seconds compared to 1440 seconds because the balance continued to weigh after the experiment was over for the same reason in the second dataset is 1636 when it should be 1560 seconds. In anticipation, we know that the data will show a periodicity due to the repetition of this “cycle” of rainfall and no rainfall. In addition, at the end of each "cycle" the bucket on the scale, in which the water flow was collected, was emptied as it was almost full, and that is why sudden drops in the mass of the flow were observed, and we should expect the highest uncertainties in these moments.

	Scenario 1	**Scenario 2**
Rainfall Intensity [mm/hrs]	37	47
Watershed Slope [%]	6	8

Tab. 3.2: Source parameters for kinematic wave flow

CHAPTER 4

Mathematical Model Framework

In this chapter, the mathematical model framework and its parameters are described. This work has a physically based because the mathematical models used to describe the components are based on an laboratory experiment and in such physical principles as conservation of mass and *momentum*. Engineers and scientist often need to estimate runoff rates and volumes from engaged watersheds. For some purposes, a more precise knowledge is required about the hydrologic response of a watershed. Thus, a model sensitivity to various physical factors or assumptions is needed, and physically based distributed models of runoff are becoming more widely used (Woolhiser et al., 1990).

It has been argued that the use of distributed physics-based models is the bestway of doing hydrological science, but there are still theoretical problems that need to be overcome in dealing with heterogeneity of model due to heterogeneity of: soil properties, preferential flows, and irregularities of surface flows (Beven, 2012). These heterogeneities are not still well

represented in the current generation of models, however, efforts will be made to avoid them in this project by simplifying the model.

In order to be founded the description of this chapter, the following documentation was reviewed: Bagnold (1966); Chow et al. (1996); Johnson and Miller (1997); Liggett and Woolhiser (1967); Miller (1984); Morris and Woolhiser (1980); Woolhiser et al. (1990); Woolhiser and Liggett (1967); Beven (2012); Semmens et al. (2007); Simunek et al. (2005); Stanić et al. (2017) and Liu (2019).

4.1 Development of Governing Equations

The fundamental principles to describe the behaviour of fluid flow are known as governing fluid equations which include the Continuity, Momentum and Energy Conservation equations. The Continuity equation was proposed by Leonhard Euler in the 18th century. In the same period, the Momentum equation, which describes the forces acting on a fluid was formulated by Isaac Newton. Later, the Energy Conservation equation was introduced by Daniel Bernoulli, it describes the transfer of energy within a fluid system. Over the years, the development of these equations has been a major focus in fluid mechanics research, contributing to the improvement of the application in modern engineering. In this section, we will explore the development of governing fluid equations. Before start this section some basic features of flows will be define:

Definitions

- Steady: depth and velocity at a point do not change as a function of time .i.e. there is no temporal variation $[\frac{\partial Q}{\partial t} = 0]$
- Unsteady: Depth and velocity vary with time $[\frac{\partial Q}{\partial t} \neq 0]$.

- Uniform: is a flow in which fluid particles have same velocities at each section of the channel i.e. there is no spatial variation $[\frac{\partial Q}{\partial x} = 0]$.
- Non-uniform: particles of fluid have different velocities at each section of channel $[\frac{\partial Q}{\partial t} \neq 0]$.
- Compressible: fluid density changes as it moves in a flow field $[\frac{\partial \rho}{\partial t} = 0]$.
- Incompressible: fluid density parcel does not change as it moves in flow field $[\frac{\partial \rho}{\partial t} \neq 0]$.

Although all fluids are compressible to some extend but when changes in pressure and temperature are negligible then fluids are regarded as incompressible.

4.1.1 *Reynolds Transport Theorem*

Hydrological processes transform the spatial and temporal distribution of water through the hydrological cycle, from atmospheric, underground and surface waters. The movement of water in a hydrologic system is influenced by the physical properties of the system. The hydrologic system can be visualized as a generalized control volume using the Reynolds transport theorem (or the general control volume equation).
In the description of dynamic phenomena it is possible to opt for two different approaches or reference systems.
First is the Eulerian description of the phenomenon is an inertial system centered at a fixed position in space where the fluid body is taken as a control volume. The control volume is described in space (x, y, z) as a function of time (t), it is located in a fixed frame in space through which the passage of the fluid is observed. Instead of following a single particle, we can record the flow properties at each point in space as time varies.
While the second type of description is Lagrangian, centered on one particle per fluid element, it takes material volume as its focus. In the Lagrangian

description the movement of the fluid body is described by following the movement of a single particle through space and time. However, it is very difficult to follow the trajectories of all the fluid particles in a flow, so the Lagrangian description is rarely used. The control volume approach is simpler because we need to develop a relationship between the system equations and the control volume equations.
The Reynolds Transport Theorem establishes a relationship between the variation in space and in time of any variable between these two reference systems. It takes the physical laws that normally apply to discrete masses of a substance and applies them to a fluid flowing continuously through a control volume. It is more usual to apply the concept of *continuum* in which the movement of individual particles is not followed. Since it is relatively more difficult to identify a system of fluid particles than it is to work with control volumes in a field such as fluid mechanics.
The Reynolds transport theorem relates the rate of change with respect to time of an extensive (mass-dependent) property to the external causes of this change. The theorem separates the action of external influences on the fluid, which are expressed as two components, the rate of change with respect to time of the extensional property within the control volume and the net flux of the extensional property across the control surface. The theorem relates the Lagrangian derivative of a volume integral of a system to an integral in Eulerian derivatives.

The Reynolds transport theorem states that *the rate of change of an extensive property of a fluid is equal to the rate of change of the extensive property stored in the control volume,* $\frac{d}{dt}\iiint \beta\rho \cdot d\forall$; *plus the net flux of the extensive property across the control surface,* $\iint \beta\rho \cdot V \cdot dA$. Both, B and β can be scalar or vectorial quantities. The equation governing the Reynolds transport theorem is:

$$\frac{dB}{dt} = \frac{d}{dt}\iiint (\beta\rho \cdot d\forall) + \iint \beta\rho\vec{u} \cdot d\vec{A} \tag{1}$$

Where B is the extensive property and β is the intensive property, which is the amount of B per unit mass $\beta = \frac{dB}{dM}$.

The Reynolds transport theorem is a fundamental theorem that relates the Lagrangian derivative of a volume integral of a system with an integral in Eulerian derivatives. In addition, it is used to develop and formulate the three important basic laws governing fluid motion; continuity, *momentum*, and energy equations in fluid mechanics, as shown in the following sections.

4.1.2 *Continuity Equation*

The continuity equation, formulated from the principle of conservation of mass, is applied to a volume of fluid where the mass becomes the extensive property thus applying the Reynolds transport theorem.
The principle states that the difference between the input and output rates is equal to the rate of change in storage. Substituting in equation 1, B for m, then $\beta = \frac{dB}{dM} = 1$, we obtain the Continuity equation for unsteady flow for comprenssible fluid:

$$\frac{dM}{dt} = 0$$

$$\frac{d}{dt}\iiint(\rho \cdot d\forall) + \iint \rho\vec{u} \cdot d\vec{A} = 0 \tag{2}$$

If fluid is incompressible then density is constant and we obtain:

$$\frac{d}{dt}\iiint(d\forall) + \iint \vec{u} \cdot d\vec{A} = 0 \tag{3}$$

Thus, in equation 3 the first term, $\iiint d\forall$, is the volume stored within the control volume that can be denoted as S, then the first term is, $\frac{dS}{dt}$, is the rate of storage change. The second term is the net flux, which is the difference between the inflow Q_{in} and outflow Q_{out} fluxes. Equation 3 can

be expressed in equation 4 as shown below:

$$\frac{dS}{dt} + Q_{\text{out}} - Q_{\text{in}} = 0 \tag{4}$$
$$\frac{dS}{dt} = Q_{\text{in}} - Q_{\text{out}}$$

Conservative Continuity Equation

The following equation written below is the solution to the integral for 1D compressible flows (equation 2).

$$\frac{(\partial \rho A dx)}{\partial t} - \rho(Q + q dx) + \rho\left(Q + \frac{\partial Q}{\partial x} dx\right) = 0 \tag{5}$$

The follow equation written below is another way to explain the unsteady continuity equation for incompressible fluid. Solving equation 3 for 1D we get:

$$\frac{\partial A}{\partial t} + \frac{\partial Q}{\partial x} - q = 0 \tag{6}$$

Where the first term the rate of change of storage with respect to time. The second term is is the rate of change of discharge in the flow direction, can be consider an input or output term and the third term is net lateral inflow. However, it can also be expressed as follows:

$$\frac{\partial A}{\partial t} + \frac{\partial Au}{\partial x} = 0 \tag{7}$$

Non-Conservative Continuity Equation

In addition, equation 3 can be represented in conservative form. This form is used, for example, in some methods of solving the Saint-Venant equations. Instead of using Q the variable is V, average velocity of the fluid.

Considering an infinitesimal volume of fluid, the law considers that the fluid entering the control volume on each face and the fluid leaving it determines the mass change that occurs within the control volume. Generally, the fluid is considered to be incompressible, with a velocity gradient within the control volume. As a result, if equation 5 is taken, and the lateral inflow is neglected the equation in non-conservative form is:

$$\frac{\partial(\vec{u} \cdot A)}{\partial x} + \frac{\partial A}{\partial t} = 0 \tag{8}$$

In 3D, x, y and z, the equation results:

$$\frac{\partial \rho}{\partial t} + \frac{\partial(\rho u_i)}{\partial x} + \frac{\partial(\rho u_j)}{\partial y} + \frac{\partial(\rho u_w)}{\partial z} = 0 \tag{9}$$

Since incompressible fluids experience no change in density with respect to time or space, the partial derivative of density with respect to time becomes zero. The equation then becomes only a divergence of velocity equal to zero.

$$\frac{\partial(u_i)}{\partial x} + \frac{\partial(u_j)}{\partial y} + \frac{\partial(u_w)}{\partial z} = 0 \tag{10}$$

$$\nabla \cdot \vec{u} = 0 \tag{11}$$

4.1.3 *Momentum Equation*

To understand the momentum conservation equation by applying an Eulerian approach to a fluid body, it is assumed that a fluid control volume fixed in space and is subjected to body and surface force applications. Equation could be expressed as the balance among the inertial force and the sum of the external forces acting on the body. The development of the momentum equation involves Newton's second law, which states that force applied on any object is equal to the time rate of change of *momentum*. Since

momentum equals mass times velocity, and mass is assumed to be constant, the equation becomes force equals mass times acceleration [$F = M \cdot a$].
In momentum equation the extensive property is $B = m\vec{u}$ and the intensive property is $\beta = \frac{dB}{dM}$. According to Newton's second law, the rate of change of *momentum* with respect to time is equal to the net force applied in a given direction. Therefore, $\frac{dB}{dt} = d(M\vec{u})dt = \sum \vec{F}$, substituting in equation 3, we have the momentum equation for non-uniform unsteady flow:

$$\sum \vec{F} = \frac{d}{dt} \iiint (\vec{u}\rho d\forall) + \iint \vec{u}\rho\vec{u} \cdot d\vec{A} = 0 \tag{12}$$

Non-uniform flow, means that the velocity varies in space. If there is a non-uniform and unsteady flow is means that the temporal derivative in equation 11 is erased, obtaining:

$$\sum \vec{F} = \iint \vec{u}\rho\vec{u} \cdot d\vec{A} = 0 \tag{13}$$

In equations 11 and 12 the two momentum terms, the one on the left represents the rate of change of *momentum* storage in the control volume, and the one on the right, the net outflow of *momentum* through the control surface, respectively.
For steady uniform flow the velocity is equal in all points of the control surface, the integral on control surface is 0, all forces are on the system are in equilibrium [$\sum \vec{F} = 0$].
Solving the first term of equation 11 in 1D, the rate of change of the momentum stored in the control volume is calculated knowing that the elementary volume in the channel is Adx, so the *momentum* is $\rho Adx\vec{u}$ or what is the same as ρQdx; so it results:

$$\frac{d}{dt} \iiint (\vec{u}\rho d\forall) = \rho \frac{\partial Q}{\partial t} dx \tag{14}$$

The second term, the net flux of momentum, is calculated by sum of entries and exits (main and lateral flows). This term is calculated using a momentum correction factor γ, also known as the Boussinesq coefficient, which takes into account the non-uniformity of the velocity distribution along the cross section of the channel. The net momentum flux in 1D can be calculated as:

$$\iint \vec{u}\rho\vec{u} \cdot d\vec{A} = -\rho \left[\gamma u_{\mathrm{x}} q - \frac{\partial(\gamma u Q)}{\partial x} \right] dx \tag{15}$$

The *momentum* equation, can be described in a more complex way if more terms are added. Is composed by a total of 5 terms such as: local acceleration, convective, pressure force, gravity force and friction force terms.

Conservative Momentum Equation

Substituting the force terms in equations 13 and 14, simplifying and rearranging, the conservative form is obtained:

$$\frac{\partial Q}{\partial t} + \frac{\partial \gamma Q^2/A}{\partial x} + gA\left(\frac{\partial y}{\partial x} - S_o + S_f + S_e\right) - \gamma q u_x + W_f Q = 0 \tag{16}$$

An easier way to represent the equation is by neglecting the terms related to lateral flow (q), wind shear (W_f), eddy losses (S_e) and assuming that Boussinesq coefficient (γ) is equal to 1 as below is shown:

$$\frac{1}{A}\frac{\partial Q}{\partial t} + \frac{1}{A}\frac{\partial}{\partial x}\left(\frac{Q^2}{A}\right) + g\frac{\partial y}{\partial x} - g(S_o + S_f) = 0 \tag{17}$$

Non-Conservative Momentum Equation in 1 dimension

$$\frac{\partial u}{\partial t} + u\frac{\partial (u)}{\partial x} + g\frac{\partial (y)}{\partial x} + g\left(S_o - S_f\right) = 0 \tag{18}$$

Where for both, equations 17 and 18:

- First term is the local acceleration force, which describes the change in momentum due to the change in velocity with time
- Second term is the convective acceleration force, which describes the change in momentum due to the change in velocity along the channel
- Third term is the pressure force, which is proportional to the change in water depth
- Fourth term is the gravity and frictional force which are proportional to the slope of the bed (S_o) and to the friction slope (S_f), respectively.

4.2 Navier-Stokes Equations

A number of mathematical models are available that have been developed to describe fluid flow, the most general of are the 3D Navier-Stokes (NS) equations. Those equations express mathematically the conservation of *momentum* for Newtonian fluids, fluids with a linear behaviour between viscosity and velocity gradient. NS equations predict the behaviour of a viscous compressible fluid in three dimensions (local components, instead of averages values), with them we are able to solve the velocity components, three equations for three unknowns. These equations need to be used in conjunction with a continuity equation to obtain the local pressure component. These equations assume that fluids obey continuum assumptions i.e. fluids are continuous rather than being discrete and fluid properties like pressure, velocity, density varies continuously from one point to another.

The Navier-Stokes equations are a set of four non-linear three dimensional partial differential equations (one is mass and three are moment equations), so there is no general solution for this set of equations.

In order to solve them, it is necessary to resort to numerical analysis to determine an approximate solution. In practice, when forming a mathematical model, many assumptions are made to simplify the problem under consideration, and the most basic equations that will capture the required phenomena are used.

Momentum *Equations*

$$\rho\left(\frac{\partial u}{\partial t}+u_x\frac{\partial u_\mathrm{x}}{\partial x}+u_y\frac{\partial u_\mathrm{x}}{\partial y}+u_z\frac{\partial u_\mathrm{x}}{\partial z}\right)=\rho{\cdot}g{\cdot}x-\frac{\partial \rho}{\partial x}+\mu\left(\frac{\partial^2 u_\mathrm{x}}{\partial x^2}+\frac{\partial^2 u_\mathrm{x}}{\partial y^2}+\frac{\partial^2 u_\mathrm{x}}{\partial z^2}\right)+\rho g_\mathrm{x}$$

$$\rho\left(\frac{\partial u}{\partial t}+u_x\frac{\partial u_\mathrm{y}}{\partial x}+u_y\frac{\partial u_\mathrm{y}}{\partial y}+u_z\frac{\partial u_\mathrm{y}}{\partial z}\right)=\rho{\cdot}g{\cdot}y-\frac{\partial \rho}{\partial y}+\mu\left(\frac{\partial^2 u_\mathrm{y}}{\partial x^2}+\frac{\partial^2 u_\mathrm{y}}{\partial y^2}+\frac{\partial^2 u_\mathrm{y}}{\partial z^2}\right)+\rho g_\mathrm{y}$$

$$\rho\left(\frac{\partial u}{\partial t}+u_x\frac{\partial u_\mathrm{z}}{\partial x}+u_y\frac{\partial u_\mathrm{z}}{\partial y}+u_z\frac{\partial u_\mathrm{z}}{\partial z}\right)=\rho{\cdot}g{\cdot}z-\frac{\partial \rho}{\partial z}+\mu\left(\frac{\partial^2 u_\mathrm{z}}{\partial x^2}+\frac{\partial^2 u_\mathrm{z}}{\partial y^2}+\frac{\partial^2 u_\mathrm{z}}{\partial z^2}\right)+\rho g_\mathrm{z}$$

Continuity Equation

$$\frac{\partial \rho}{\partial t}+\frac{\partial u_\mathrm{x}}{\partial x}+\frac{\partial u_\mathrm{y}}{\partial y}+\frac{\partial u_\mathrm{z}}{\partial z}=0$$

4.3 Sallow Water Equations

The flow of water over the surface of a basin is a complex process that varies in all three spatial dimensions and in time. It can be observed as a distributed process in which flow, velocity, and depth or height vary in space and time. The flow begins when water stored at the surface becomes high enough to overcome surface retention forces and begins to flow. Two types of basic flows can be distinguished: overland flow or channel flow. Overland flow or runoff is a thin layer that flows across a wide surface.

Channel flow a narrower stream that flows in a confined path.
In open channel flow, the most commonly used models fall into the classification of shallow water or overland flow equations. As already mentioned, shallow water flow is defined as the depth of the water being small compared to the horizontal reach of the water, that is, it is assumed that the flow is relatively shallow to the dimensions of the width of the cross-sectional area, as is the case in this project.
Superficial water flow is governed by the principles of continuity and momentum. The application of these principles to non-permanent three-dimensional flows on the surface of a basin is only possible under very simplified conditions, therefore they are generally assumed in one-dimensional and two-dimensional flows. The shallow water or overland equations are a set of partial differential equations derived from depth integration of the Navier-Stokes equations. This is done, as said before, in the case where the horizontal length scale is much larger than the vertical length scale. Under this condition, the conservation of mass implies that the vertical velocity scale of the fluid is small compared to the horizontal velocity scale. Shallow water equations in unidirectional form are also called Saint-Venant equations.

4.4 Saint Venant Equation

In the case of modelling predominantly one spatial dimensional flows, the Saint Venant equations are the most widely used system for solving transient flow problems in open channels and surface runoff. There are a number of computer models capable of solving them, like HEC-RAS, ISIS and Flood Modeler; as they have a wide variety of applications: the assessment of flood risk reduction measures, dam breaks analysis, storm pulses in an open channel, as well as storm runoff in overland flow.

In 1871, Barre de Saint Venant presented the equations describing unsteady one-dimensional (1D) shallow water flow in an open channel, consisting of Conservation of Mass and *Momentum* equations.
These equations are a pair of partial differential equations of unsteady flow, in which the dependent variables are discharge, Q [m^3/s], and depth, h [m]. The independent variables are the distance along the channel, x [m], and time, t [s]. The solutions of these equations provide the discharge-time and depth-time relationships along the channel.
The Saint Venant equations describe the gradually varying flow of an incompressible, inviscid fluid and consist of a set of integral or differential equations composed by, continuity or mass equation (equation 2), and an equation of motion (equation 11) that is formed by applying Newton's second law of motion along the channel.

To model those channels, the flow is treated as a one spatial dimension and the model must contain some fundamental assumptions or statements:

- The one-dimensional flow assumption, 1D, means that velocity and depth vary only in the longitudinal direction. It means, there is only one depth value at any point along the channel, so the water level along the cross section is horizontal. This implies that the velocity is constant or uniform over a cross section, and also the velocity not vary with depth.

- The flow is assumed to vary gradually along the channel, this implies that the vertical component of the acceleration of the fluid is negligible. Hence, the streamline curvature is small, and the pressure variation with depth is hydrostatic. When the vertical acceleration is negligible implies that the velocity is uniform across the cross section and does not vary with depth.

- The friction and turbulence can be represented using the same empir-

ical laws that govern uniform Steady-state flow, such as Manning's equation.

- It could also be assumed that the slope is gentle. The bed slope is small resulting in the cosine of the angle between the bed level and the horizontal being approximately unit, so scour and deposition effects are negligible.
- As we are dealing with water the final assumption is that the fluid is in-compressible and the density is constant throughout the flow.

As the equations are non-linear the general analytical solutions are not possible for most conditions. Analytic solution have been restricted to limited regions of the solution domain or to special cases where suitable simplifications could be made. So we have to resort to numerical methods, thus we could evaluate discharge and depth at discrete points along the length of the channel at discrete times (Hsu, 2018).
Concluding the 1D Saint Venant equations are: 6 and 17 in their conservative form and, 8 and 18 non-conservative form, which are collected below:

$$\frac{\partial A}{\partial t} + \frac{\partial Q}{\partial x} - q = 0 \tag{6}$$

$$\frac{\partial(\vec{u} \cdot A)}{\partial x} + \frac{\partial A}{\partial t} = 0 \tag{8}$$

$$\frac{1}{A}\frac{\partial Q}{\partial t} + \frac{1}{A}\frac{\partial}{\partial x}\left(\frac{Q^2}{A}\right) + g\frac{\partial y}{\partial x} - g(S_o + S_f) = 0 \tag{17}$$

$$\frac{\partial u}{\partial t} + u\frac{\partial(u)}{\partial x} + g\frac{\partial(y)}{\partial x} + g\left(S_o - S_f\right) = 0 \tag{18}$$

4.5 Kinematic Wave

The first Kinematic-wave approximations to equation 37 were first named and described in detail by Lighthill and Whitham in 1955 (Miller, 1984). Eagleson in 1970 was further with the development of this work, he gave analytical solutions for the case of constant effective rainfall input. Later, numerical solutions have been used in a series of rainfall-runoff catchment models based on the infiltration mechanism of excess surface flow runoff, the best known is probably KINEROS (Beven, 2012). Since about 1970, the kinematic wave approximation has become a widely used method to simulate the movement of rainfall excess water over the land surface and through small channels (Woolhiser et al., 1990).

The dynamic-wave model describes one-dimensional shallow-water waves (unsteady, gradually varied, non-uniform, open-channel flow) and consists of the solution of the Saint-Venant equations with appropriately prescribed initial and boundary conditions.

In most approximations of dynamic waves, which describe unsteady non-uniform flow, the continuity equation and an approximation of the equation of motion are solved. But some simplifications could be done to make the treatment of equations easier to solve. The kinematic-wave model is one of a number of approximations of the dynamic-wave model (Saint-Venant equations). The Kinematic wave do not preserve all of the properties of the more complex equations, such as backwater and diffusive wave attenuation (due to infiltration).

When the source terms, the bed slope and the friction terms are much larger than the first three terms in the *momentum* equation, a simplification could be done in the *momentum* equation by ignoring the first three terms that are assumed to be insignificant. This model assumes that the friction slope is equal to the bed slope, it means gravitation and shear forces are significant whereas local acceleration, convective acceleration and hydrostatic pressure forces are not (Johnson and Miller, 1997). Then, in

the *momentum* equation in this case is governing by gravity and frictional forces those forces are balanced, and the inertial force and pressure terms are neglected. This approximation implies Steady uniform flow and that the friction slope is approximately equal to the slope of the channel.

This simplifies the full Saint-Venant equation to the kinematic wave, where the momentum equation becomes:

$$g(S_\mathrm{f} - S_\mathrm{o}) = 0 \tag{19}$$

$$S_\mathrm{f} = S_\mathrm{o}$$

Viewed at a microscale, overland flow is a complex three-dimensional process, but a larger scale it can be viewed as one-dimensional flow, which flux or discharge per unit width (q) is proportional to some power to the storage per unite area or depth if the surface is a plane (h). Thus, it follows that q is a function of y or A, the rating curve is used because it is a relation between stage (river level) and streamflow (discharge). Then q can be evaluated using any of the uniform flow equations, such as the Chezy or Manning formulas, in which S_o is substituted for S_f.

$$Q = \alpha A^m \tag{20}$$

In open channel flows, the velocity is determined using the Chezy and Manning formulas, which are derived from the Darcy-Weisbach equations to calculate head losses due to friction.

$$\text{Chezy: } u = c\sqrt{RS_\mathrm{f}}$$

$$\text{Manning: } u = \frac{R^{2/3} S_\mathrm{f}^{1/2}}{n}$$

In which α and m are coefficients defined for each channel cross section,

related to slope, surface roughness and flow regime. The parameters related to the roughness of the catchment, $\alpha and m$ can be described using the Manning hydraulic resistance law:

$$\alpha = \frac{\sqrt{S_o}}{n}; \text{ and } \mathbf{m} \text{ is our case is equal } \frac{5}{3} \tag{21}$$

When a channel is prismatic and rectangular, it means that the cross-section along the channel and the slope of the riverbed are constants, then in equation 6 can be modified. The unsteady continuity equation (equation 6), in a watershed that is a prismatic channel where it is written $\frac{\partial A}{\partial t}$ is replaced by $bw \cdot \frac{\partial h}{\partial t}$ and, the discharge could be replaced by $Q = bw \cdot q$. Obtaining an alternative form, substituting these relationships into equation:

$$\frac{\partial q}{\partial x} + bw \cdot \frac{\partial h}{\partial t} = 0 \tag{22}$$

Equation 20, as we said before, can be rewritten:

$$q = \alpha \cdot h^m \tag{23}$$

The final continuity equation for kinetic wave is going to be, the same as equation 22 but we include the term the effective rainfall [r(t)], which is the lateral inflow rate and substituting the bottom width by 1, which is our case, the obtained equation is:

$$\frac{\partial q}{\partial x} + \frac{\partial h}{\partial t} = r(t) \tag{24}$$

A combination between equation 23 and 24 was done, to get the overland equation flow:

$$\frac{\partial \alpha \cdot h^m}{\partial x} + \frac{\partial h}{\partial t} = r(t) \approx q_{\text{out}}(x,t) \tag{25}$$

If we rewrite the same equation we obtain the analytic solution for kinematic wave:

$$\frac{\partial h}{\partial t} + \alpha \cdot m \cdot h^{m-1} \frac{\partial h}{\partial x} = r(t)$$

$$\frac{\partial u}{\partial t} \approx \frac{\partial h}{\partial t} = -\alpha \cdot m \cdot h^{m-1} \frac{\partial h}{\partial x} + r(t) \tag{26}$$

Thus, the kinematic-wave model is described by the continuity equation and a uniform flow equation plus the usually imposed initial and boundary conditions. A definition sketch of one-dimensional flow on a plane surface is shown in figure 4.1.

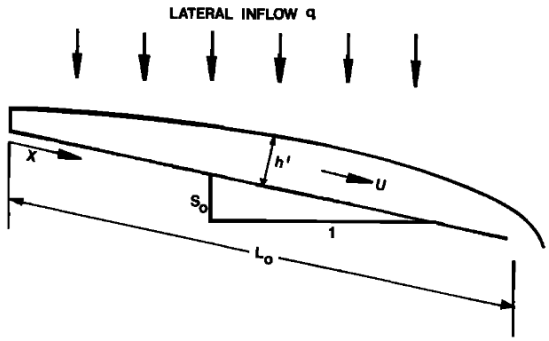

Fig. 4.1: Sketch of overland flow on a plane by Morris and Woolhiser (1980)

In order to run a simulation define some conditions is need it, for example, an initial and two boundaries conditions, know discharge out of the channel or depth downstream.

4.6 Contaminant Transport Equation

To analyse the movement of water and solutes in a fully saturated medium, the equation that obeys this type of flow is Richard's 1931 advection-dispersion solute transport equation for unsaturated medium. The Richards equation expresses the Darcian flow in a variably saturated porous medium, where the flow originates from pressure and gravitational forces. The advective part of the water flow model can consider both Dirichlet (head pressure) and Neumann conditions (prescribed flows). Once we know the advection term due to the solution of the kinematic wave, the pollutant transport can be calculated, in this case ash.

During the last century innumerable flume experiments have been done, and a multitude of theories have been published in attempts to relate the rate of sediment transport by a stream of water to the strength of the water flow (Bagnold, 1966).

The solute transport equations take into account advective-dispersive transport in the liquid phase, which is numerically solved by the Richards equation for variably saturated water flow and the advection-dispersion solute type equations (Simunek et al., 2005).

The general equation used to describe the sediment/solute dynamics eroded by flowing water at any point along a surface flow path is a mass balance equation similar to that for kinematic water flow (Woolhiser et al., 1990). In the solute transport equation in shallow water can be assumed to be vertically well-mixed solute being transported by depth-averaged flows and their dynamics can be described by equation 27 for horizontal advection (1D) transport equation for substance (Liu, 2019; Stanić et al., 2017), that is considered an ideal tracer. Equation can be described as follows, when the third term related to the dispersion coefficient (D) will be neglected and the effective velocity $u_{eff.}$ is advection term already determined (eq.26):

$$\frac{\partial C}{\partial t} = -\frac{\partial u_{eff.} C}{\partial x} + D\frac{\partial^2 C}{\partial x^2} \tag{27}$$

CHAPTER 5

Results and Discussion

First, the data transformation and data analysis is explained in section 5.1. The simulation part is continued and we begin to approach the calibration using expert knowledge, this is explained in the section reference 5.2.1. It continues with the developing of calibration algorithms to achieve the parameterization of our objective function which is explained in section 5.3. Finally, the results of the model calibration are shown and discussed in section 5.4.

5.1 Data Analysis

In this chapter R software is used as a work tool to analyze the data. R is an Open Source environment for statistical computing and graphics 'not unlike' version 3 of the S system developed at Bell Laboratories. R is an advanced statistical computing system with very high quality graphics that is freely available for most computing platforms, the project was started by Ross Ihaka and Robert Gentlemen at the University of Auckland (Ripley et al., 2001).

5.1.1 Data manipulation and transformation

In order to determine the kinematic curve (equation 26), it is necessary to determine α, which in turn is related to the n, Manning roughness coefficient (equation 21). Due to this, as explained in 3.1.4.2, an experiment test was developed, in it the data collected were the cumulatively outflows of the study watershed.

Therefore, a scale was placed with a container, and each time this container was filled, it was removed from the scale and replaced by another. Hence, the measurements collected have the following structure [Fig.5.1].

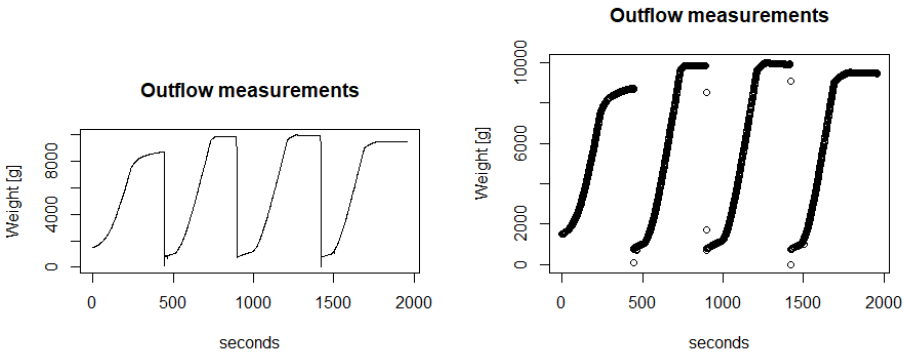

Fig. 5.1: First observation of raw data

That is why a repositioning of the data structure is necessary, trying to avoid the disturbance due to this influence, is done manually with for loops in R [Fig.5.2].

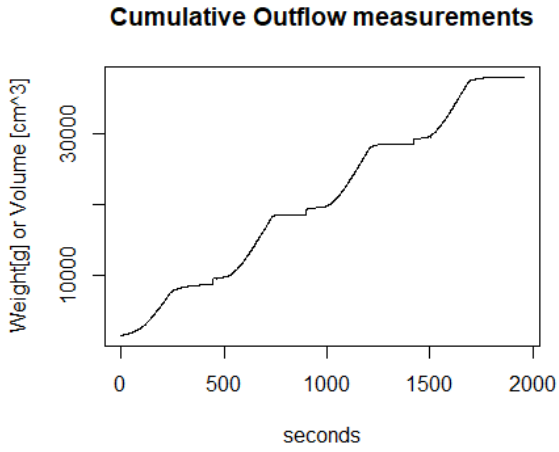

Fig. 5.2: Relocation of measurements

Moreover, with the cumulative flow function formed by taking the derivative of this, the flux of flow is obtained at each instant. In order to do that, a "for loop" was used again [Fig5.3].

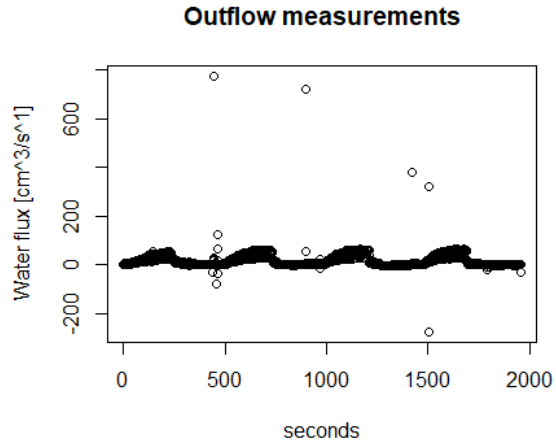

Fig. 5.3: Flux measurements derived from derivative of Cumulative Flow

Since the data represented contains outliers and, negative values, which have not a valid physical representation, these uncertainties should be removed. They are detected especially at the junction points of the cumulative curve, which coincide with sudden changes in flow, where there are inflection points.
The negative values were eliminated and using the boxplot.stats and ecdf R functions, it was chosen to eliminate the fluxes greater than 125 and 110 cm^3s^{-1} for first and second scenario respectively. With the Empirical Cumulative Distribution Function (ECDF), is used to display the data points in a sample from lowest to highest against their percentiles. So using this function with the previous values it is known that the 99.69002% and 100% of the data is still collected, respectively [Fig.5.4].

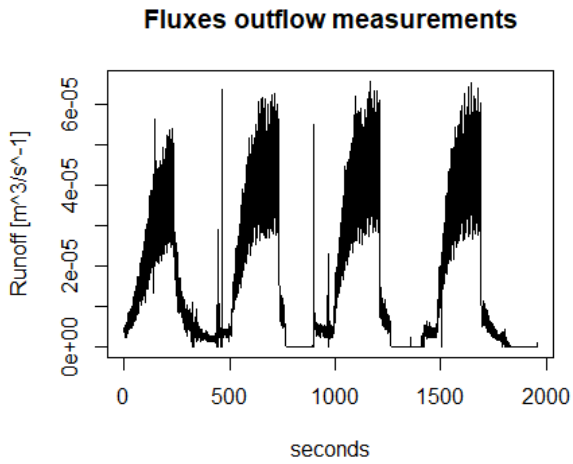

Fig. 5.4: Flow measurements after removing outliers

Afterwards, this step is followed by the unit change from cm^3s^{-1} to m^3s^{-1} dividing by 1^{-6}. In the same way, the change of units for the cumulative flows from grams to tons is also carried out.
Furthermore, as can be seen in the graph, the output flow has a large

fluctuation, so it will be necessary to perform a smoothing of the function. This was done by means of the "smooth function" in R and the classic method of moving averages, two methods that were compared [Fig.5.5].

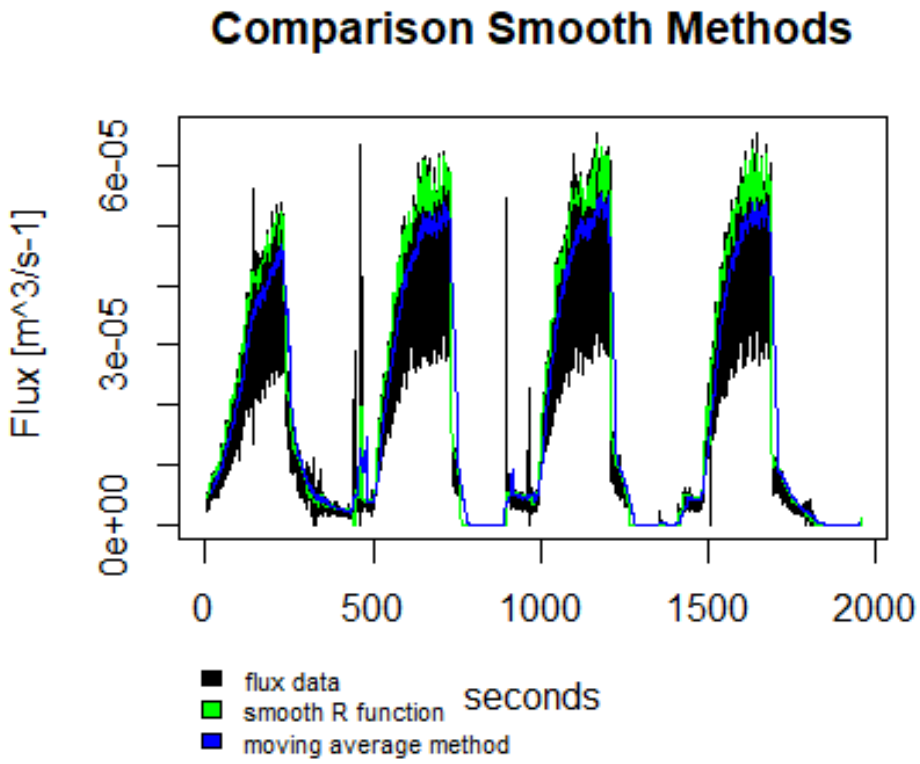

Fig. 5.5: Comparison of data smoothing methods

Lastly, the following figures show the filtered laboratory data, both cumulative and fluxes of both scenarios, already optimal to continue with the analysis of results.

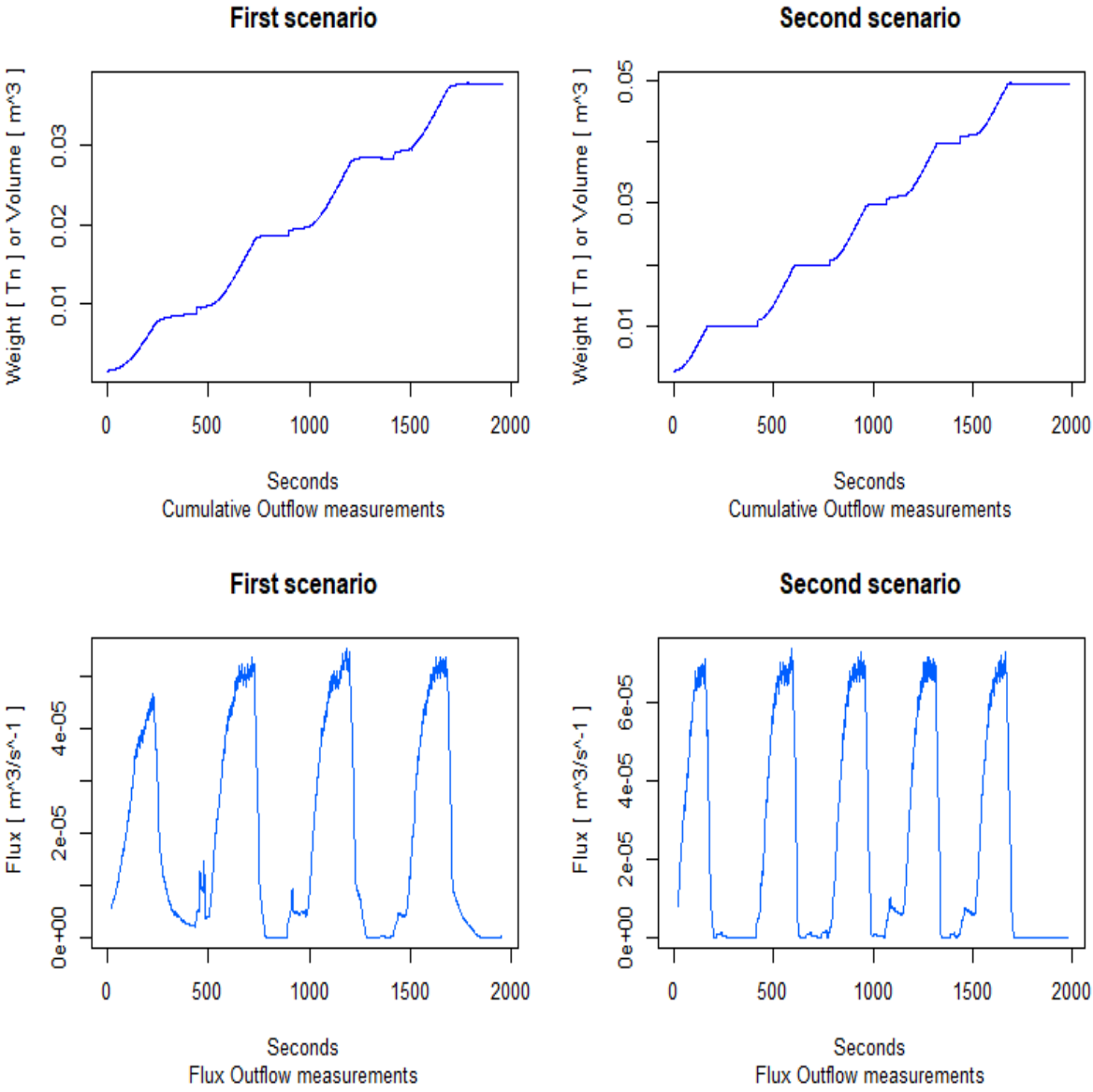

Fig. 5.6: Laboratory measurements filtered and smoothed

5.2 Numerical Solution- Simulation with DRUtES

In this section, it was carried out the simulation of the model by solving the kinematic wave (equation 26) with the help of the DRUtES software (Dual Richards Unsaturated Equation Solver). The simulation results are computed with a forward finite-difference method solution scheme that proceeds by replacing the derivatives in the equation by finite differences (Cheney and Kincaid, 2012).

Fully three-dimensional models for surface and subsurface flow processes have become computationally feasible but most current physically based distributed rainfall–runoff models still discretise the catchment into lower dimension subsystems, such a discretisation leads to only approximate representations of the processes and may lead to numerical problems in some cases (Beven, 2012).

In our project, these simplifications is made using simpler solutions based on the kinematic wave equation for surface flow. As it mentioned above, it is nearly always not possible to obtain analytical solutions to the nonlinear differential equations describing hydrological flow processes.

The approximate numerical solution of nonlinear differential equations is, in itself, a specialty in applied mathematics, which must be left in the hands of experts since writing algorithm solutions can lead to producing innacurate or inconsistence algorithms (for instance, that do not converge to the solution of orginial equation) or that are unstable. A stable solution means that any small errors due to the approximate nature of the solution will be damped, while an unstable solution means that those small errors will be amplified (Beven, 2012).

DRUtES is a finite element solver for coupled nonlinear parabolic problems, namely the Richards equation with the dual porosity approach (modeling the flow of liquids in a porous medium). It presents an algorithm for the automatic selection of time steps, since the proper duration of the time step is crucial to achieve the accuracy of the Euler time integration method

(Kuráž and Mayer, 2013).
The simulation results are represented in this section, first is shown an approach the calibration using expert knowledge 5.2.1 and then, it continues with developing of calibration algorithms 5.3.

5.2.1 First approach to Calibration - Applying Expert Calibration

In the following section it will be observed how the response of the model varies, the simulated curve under the influence of the parameters to be determined. It will be observed which is the approximate range of the parameters to be determined, precipitation intensity and Manning's roughness coefficient. It must be known how each parameter influences the result of the model, for this we will use our knowledge by performing a manual sensitivity analysis.
Some animated figures have been introduced in this document, figures 5.12, 5.13 and 5.9, to be able to see the influence of these parameters in the flow, however to be able to execute, note that these animations currently only work with Acrobat Reader 6 or later, and javascript should be enabled.

5.2.1.1 The Effects of Parameters on Model outputs

This part shows the effects of the intensity parameters and Manning roughness coefficient on the results of the mathematical model of the kinematic wave. To do this, the value of the parameters, intensity and/or Manning roughness coefficient is changed and the model is run several times to investigate how each parameter affects the model output. With this investigation the following results are obtained.

Influence of Manning roughness coefficient
Increasing the Manning's roughness coefficient increases the energy loss

due to increased frictional or shear force, this is because the slope bed is rougher and imposes more resistance to the flow. The simulations fluxes are presented in blue meanwhile the measured flux is in black.
As can be seen in the following figures where the precipitation intensity was fixed at 30 mm, by increasing the Manning's coefficient, the peak flow shifts in time, i.e. it influences the advective/convective term, delaying the response in time. In addition, it is observed that the maximum or peak value of the fluxes decreases, flattening the curve, and the fluxes become more homogeneous. The fluxes become more "linear" with less variation as the Manning's coefficient increases. While, in the examples where Manning's coefficient value is lowest the response to rainfall cycles or patterns is best reflected.

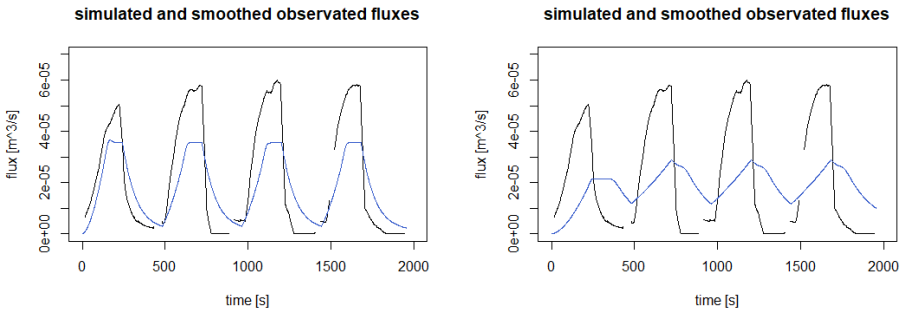

Fig. 5.7: Influence in fluxes of Manning roughness coefficient, n = 0.135 and 0.48 $[s/m^{1/3}]$, on left and right figures respectively

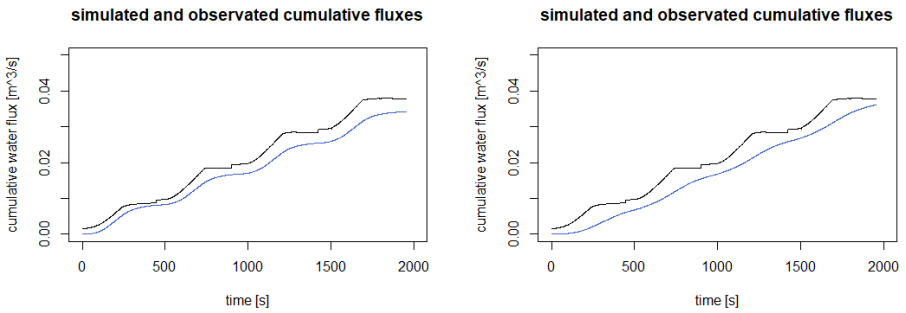

Fig. 5.8: Influence in cumulative fluxes of Manning roughness coefficient, n = 0.135 and 0.48 $[s/m^{1/3}]$, on left and right figures respectively

The same is reflected in the cumulative flow graphs, as roughness coefficient increases the flow is more "stable", the precipitation/non-precipitation cycles lose influence. Likewise, at high roughness coefficients it is observed that the cumulative flux at the end of the experimental time is higher, while at the beginning it has lower values than for a lower n. Moreover, in other words, the lower the roughness coefficient, the more similar the simulation and original curves become, so that the response to the precipitation/non-precipitation cycles is more accurately reflected when n is smaller.

In general, as the Manning's coefficient increases, the hydrograph flattens out, the runoff slows down, the peak flow decreases and the arrival of the peak hydrograph is delayed. As the resistance of the substrate is greater, the advective flow peaks take longer time to achieve the gauging control and are also attenuated, with a smaller size. The Manning's roughness coefficient, which tells you how rough a surface is, influences the magnitude of the flows and their spatio-temporal distribution.

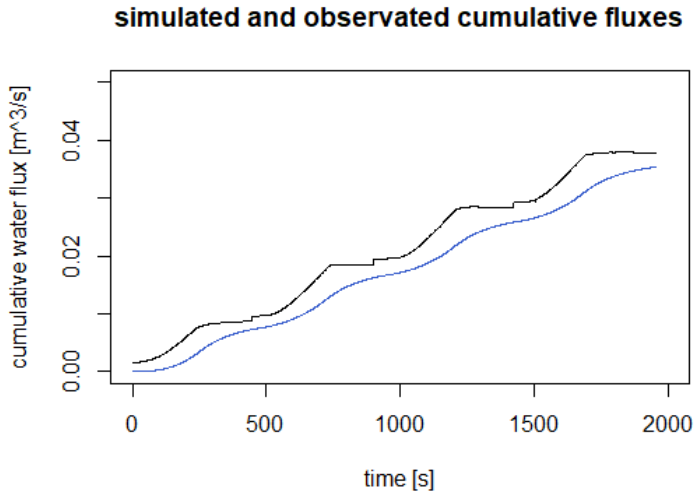

Fig. 5.9: Influence in fluxes of Manning roughness coefficient from n = 0.30 to n = 0.36 mm $[s/m^{1/3}]$ with fixed Rainfall intensity in 30 [mm]

Influence of Intensity Effective Rainfall [mm]

The influence of rainfall intensity on cumulative and not cumulative flows at the outlet of the study watershed can be seen in the following figure 5.10 and 5.11, where the simulation flows are shown in blue, while the measured flow is shown in black.

A constant roughness coefficient was set at 0.265 $[s/m^{1/3}$ to be able to observe the influence of precipitation. At higher intensity of rainfall, it is observed how the flow values increase in a potential way, the flux become more pronounced, changes are more rapidaly. The intensity of the precipitation does not influence the advective term, in the spatio-temporal distribution of the flows.

In the figures of cumulative flows, the same thing is observed, there is no variation in the shape of the function, but yes when increased the intensity of the rain, since a greater amount of water is being introduced, this causes the values of the function to increase, and presents a greater volume of flow

at the end.

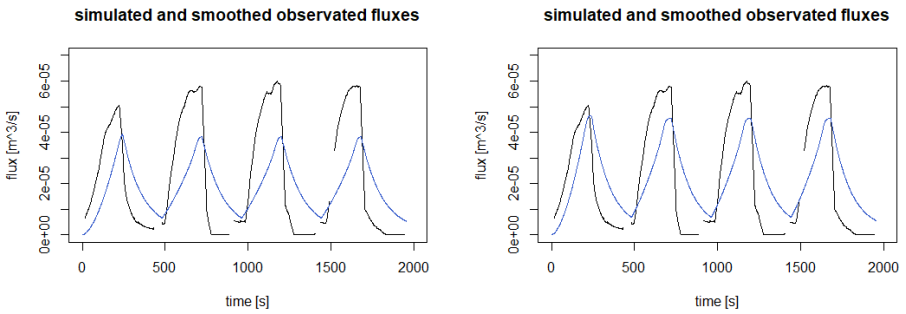

Fig. 5.10: Influence in fluxes of Rainfall intensity [mm] from 30 mm to 36 mm with Manning roughness coefficient fixed

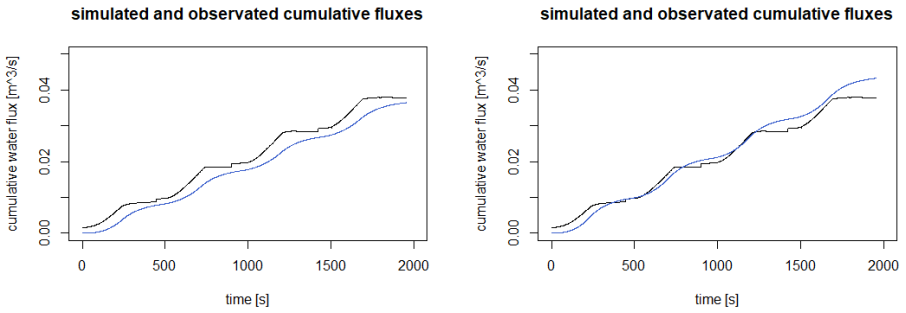

Fig. 5.11: Influence in fluxes of Rainfall intensity [mm] from 30 mm to 36 mm with Manning roughness coefficient fixed

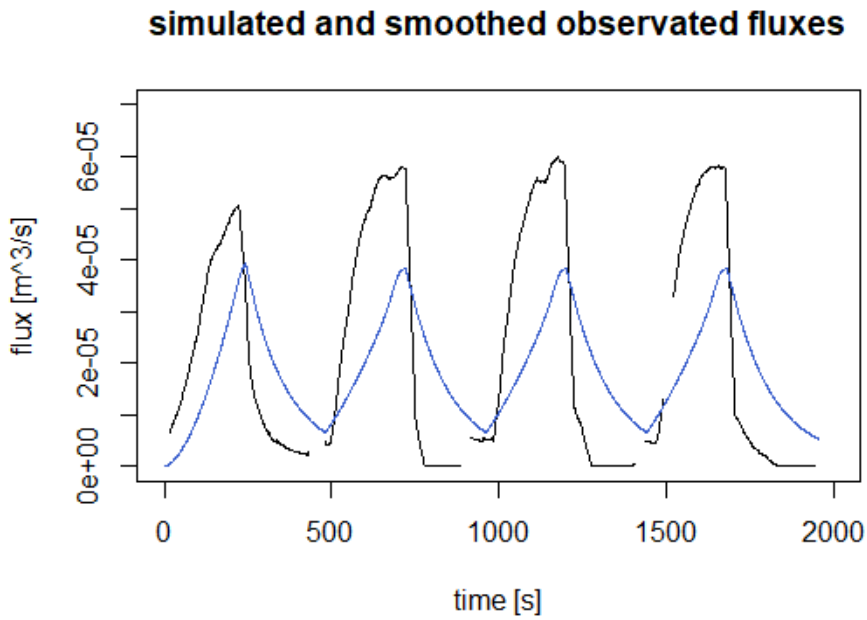

Fig. 5.12: Influence in fluxes of Rainfall intensity [mm] from 30 mm to 36 mm with Manning roughness coefficient fixed

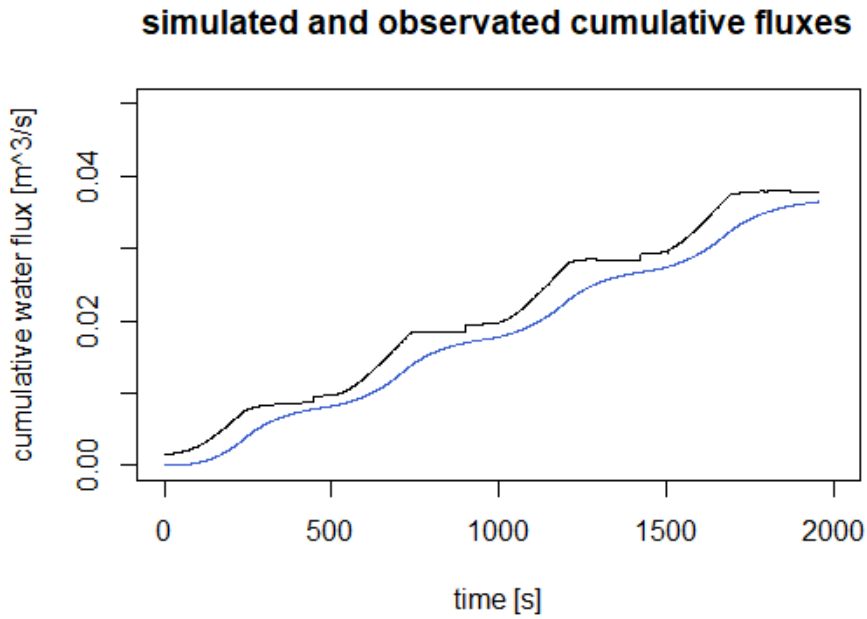

5.3 Inverse Modelling

Inverse modeling, is an approach that attempts to find the unknown parameters that best explain a set of observed data. This minimization of the deviations between the predicted observed data is done by altering the parameters of the reference model. Unlike forward modeling, which involves simulating a system to predict how it will behave in the future, inverse modeling uses data from the past to go back and determine the parameters that led to the observed results. It is called an inverse problem because it starts with effects and then calculates causes. Inverse problems are important mathematical problems in science and mathematics because after a field/laboratory experiment they tell us about parameters that we cannot observe directly.
Optimization techniques have been applied to the solution of engineering and mathematical problems for many years, is an essential task in many computational problems. In statistical modelling for instance, in the absence of analytical solution, maximum likelihood estimators are often retrieved using iterative optimization algorithms which locally solve the problem from given starting values (Philipps et al., 2020).

5.3.1 Objective Function Definition

Having the data observed in the laboratory, knowing the slope of the basin, the value of the effective rain intensity and Manning roughness coefficient parameters will be determined. To do this, the flow will be simulated using DRUtES and later, with optimization algorithms, it will be pursued that the difference between the simulated and measured values in the laboratory is minimal.
To find the function that best fits for each scenario, the objective function is used. The objective function defines a relationship between the values of the real functions obtained in the laboratory and the simulated ones, which in

our case will be the RMSE (equation 27). The goal of optimization is to find the values of the variables that minimize the result of the objective function.

$$RSME = \sqrt{\frac{\sum_{i=1}^{N} (Predicted_i - Actual_i)^2)}{N}} \tag{27}$$

5.3.2 Marquardt-Levenberg algorithm

In this section what we do is to obtain the best parameters that minimize the error between the observed values and the simulated ones, searching the value parameters that minimize the objective function. The error function, as mentioned, is the one that expresses the mean square root error between the observation function and the simulated function (equation 27). Therefore, by obtaining the global minimum point in the error function, it is equal to obtaining the best simulated approximation of our measured values. To do that the *Levenberg-Marquardt algorithm* (LMA) is used, which is commonly used in iteratively optimization especially for cases of nonlinear curve fitting problems (Ranganathan, 2004) and (Pujol, 2007). The LMA is a hybrid technique that uses both *Newton-Rapshon method* (NR) and steepest or *Gradient Descendent method* (GD) approaches to converge to an optimal solution . The hybrid approach is often used to trade off the best characteristics of different algorithms to solve a wider range of problems. For example, the Gauss-Newton approach is faster than LMA if the initial guess is relatively close to the optimal solution. In the event that this is not the case, the hybrid solution (LMA) uses aspects of the steepest descent approach to traverse the design space and find a potential solution area, and then find the optimum. This technique is particularly effective in solving systems of non-linear equations (Wilson and Mantooth, 2013). Pujol (2007) developed a review of the theoretical basis described in the literature of the Levenberg-Marquardt damped least squares method.

5.3.2.1 Descent Gradient method

This method is the simplest, most intuitive technique to find minima (Ranganathan, 2004). For parameter updating, the next point is selected to evaluate the function based on the gradient of the function at the current point, and the next point in the direction of the negative gradient is selected which is steepest descent. The new point is obtained from the previous point which is going to be displaced in the opposite direction to it's gradient.

$$X_{i+1} = X_i - \lambda \nabla f(X_i) \tag{28}$$

However, simple gradient descent has certain convergence problems. It behaves inversely in terms of the speed at which it advances to the next point to be evaluated. When the slope is flat or gentle we would like to take big steps and take small ones when the slope or gradient is steep/large, so as not to rattle the minima (Ranganathan, 2004). But based on the update rule (equation 28) just the opposite occurs. Being this behaviour the major disadvantage of this method is that λ can not be constant. Because, as already mentioned when the function $f(x)$ is in flat areas, λ does not made big steps and the optimizer may get stuck in such areas, it will take a lot of time and it will be conservative. The step size is the amount of displacement. On the other hand, λ takes very big steps where the function f(x) has steep cliffs and may will pass the minimum point, we will have a lot of oscillations. So, to summarize, λ cannot be constant across iterations, because it overshoots or undershoots. This method is much more robust compared to NR but it can be very slow.
In figure 5.15, the are two possible gradient descent trajectories, in (a) the objective function is well behaved which allows the gradient to move smoothly towards the optimum while in (b) the gradient starts to oscillate as it falls into a narrow valley, thus converging more slowly. In this figure δt is the step size, f is the function and, x_t is a candidate solution of the

algorithm at time t.

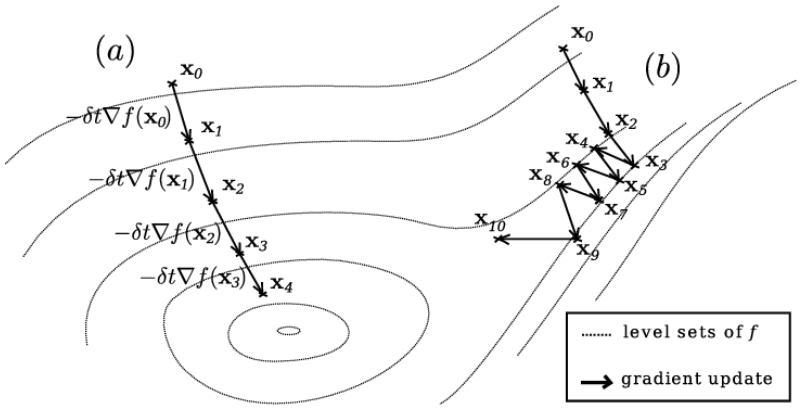

Fig. 5.14: Figure by Ludovic Arnold

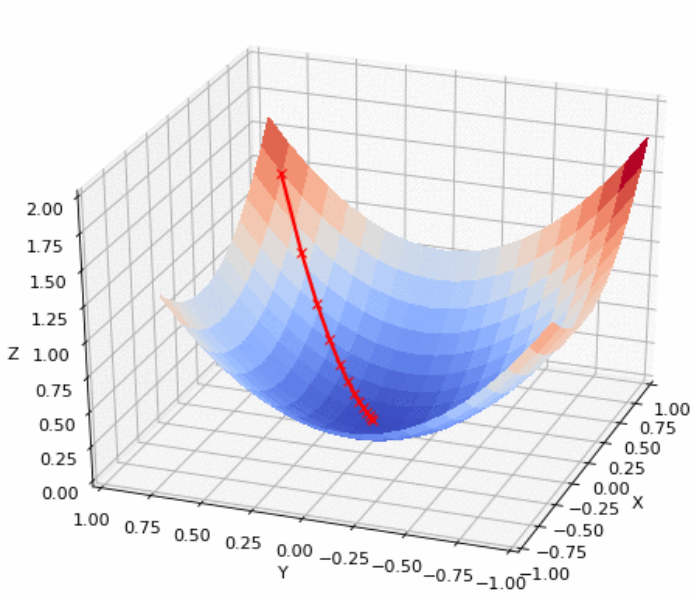

Fig. 5.15: Figure by Ayoosh Kathuria

5.3.2.2 Newton-Raphson method

This is the most famous algorithm for finding the roots of non-linear algebraic equations, is also used to find the maximum or minimum of a function (Ranganathan, 2004). This method can be used to find the minimum of the function or the stationary point of the function. The gradient of the function at the next value of $X_i + 1$, is the gradient of the function in the current point plus the difference between those two points times the Hessian matrix of the function in the current point plus other higher terms.

$$\nabla f(X_{i+1}) = \nabla f(X_i) + (X_{i+1} - X_i)^T \nabla^2 f(X_i) + \text{Higher order terms } = 0 \tag{29}$$

The idea of this method is to approximate the gradient of the next point of function to be zero, in this way we update the equation. The idea of this method is again to obtain from a point, in the iteration we want to obtain next point seeking that this new point its gradient is zero, it is a stationary point. To do this, the gradient of f at the next or new point is approximated by the Taylor polynomial of degree 1 centred on the current node or point. In this way, the disadvantage of the GD method is improved by using both the curvature and the information about the gradient, that is, the second derivatives (Ranganathan, 2004) and (Philipps et al., 2020). If we neglect the higher order terms, assuming f to be quadratic around X_i, we will have:

$$X_{i+1} = X_i - (\nabla^2 f(X_i))^{-}1 \nabla f(X_i) \tag{30}$$

In this new expression, is the subtraction from X_i the inverted Hessian matrix times the gradient of the function. This expression is going to give us the minimum of the function. This method says that if we keep updating the x according to the formula above, it should take you from wherever you star toward the stationary point.

Advantages of this method is that it converges very fast if the initial starting

point is close to the global minimum. This is because this method not only takes into account the gradient of the function, the slope of it, but it also cares about the Hessian matrix. This method used a mix of the curvature and the gradient. This method uses the inverse of the Hessian Matrix $\nabla^2 f(X_i$ or the function's curvature to reach to the minimum point. The curvature decrease the time requires to the convergence. Another advantage is when the point is in a flat area (small curvature), the curvature high gains and in sharp drops (high curvature), it has smaller gains.

However, the mayor disadvantages of this method are:

- You must star with a close initial guess, because you can get trapped in a local minimum instead of a global minimum
- when the objective function is to optimize has a concave appearance it would diverge instead of converge
- it may be have issues with Hessian Matrix it self, this could be time consuming operation in large matrices because if we don't have a function of f we need to calculate all of the partial derivatives numerically, and then inverted
- Hessian matrix, could be problematic too if there is a singular matrix, if it's determinant is equal zero, you cannot invert it
- To lead to the minimum the Hessian matrix need to be defined positive, so the eigen-values must to be positive

5.3.2.3 Combination

It can be seen that simple gradient descent and Gauss-Newton iteration are complementary in the advantages they provide (Ranganathan, 2004). The Levenberg-Marquardt method is a combination of Gradient Descent and Newton-Raphson method.

The idea of damping the solution was introduced by Levenberg, who also showed that it is possible to do that while at the same time reducing the value of a function that must be minimized iteratively (Pujol, 2007). Whereas, Marquardt started with the current equation and showed that it interpolates between the ordinary least squares method and the steepest descent method (Pujol, 2007).

The next method (equation 31) was develop by Levenberg (1944):

$$X_{i+1} = X_i - (H + \lambda I)^{-}1\nabla f(X_i) \tag{31}$$

Where: H is the Hessian matrix evaluated at X_i

Levenberg method the updates rules are: If the error goes down following an update, it implies that our quadratic assumption on f(x) and λ by a factor of 10 (reducing the influence of the gradient). But if the error goes up, the algorithm does the against, now it follow the gradient more and so λ is increased by a factor of 10 (Ranganathan, 2004).

The Levenberg algorithm is working as follows:

1. Do an update following the rule above
2. Evaluate the error at the new point
3. If the error has increased as a result of the update, then retract the step (i.e. reset the weights to their previous values) and increase λ by a factor of 10. Then go to step 1 again.
4. If the error has decreased as a result of the update, then accept the step (i.e. keep the weights at their new values) and decrease λ by a factor of 10.

The advantage of this method is that the second derivative helps to have a greater movement along the directions of the gradient when its slope is smaller, solving the valley problem presented by the GD algorithm.
The disadvantage of the above algorithm (equation 31) is when the value of λ is large, the calculated Hessian matrix is not used at all; Marquardt replaced the identity matrix in with the diagonal of the Hessian which resulted in the Levenberg-Marquardt update rule (Ranganathan, 2004), presented below:

$$X_{i+1} = X_i - (H + \lambda diag[H])^{-}1\nabla f(X_i) \tag{32}$$

When λ goes to zero, means that the second term is almost zero so the equation is going to be the Newton-Raphson equation. In the other hand, if λ is very large and goes to infinity, the second term will dominate the Hessian matrix, so the equation is going to be the Gradient Descent.
The iteration procedures is: if the new function drops λ decrease for the next iteration. If the new function is bigger than the previous one, we get uphill so we will not accept the new point and we need to redo the update, so we will change λ, we need to increase λ.

In terms of convergence speed	**In terms of converge stability**
GD $<$ LM $<$ NR	GD $\gg$ LM $\gg$ NR

Tab. 5.1: Summary of algorithm advantages

This LMA algorithm is faster than the Gradient's descent and it's slower than the Newton-Raphson method (Wilson and Mantooth, 2013), because it needs the backward forward changing λ and so on, but it is more stable than NR. As summarise this method, is a good method because it combines the speed of NR with the stability of GD and also has automatic logic for updating the λ.

5.3.3 Differential Evolution Algorithm

Differential Evolution (DE) algorithm belongs to genetic optimization algorithms that are inspired by the process of natural selection using operations of crossover, mutation, and selection on a population in order to minimize an objective function over the course of successive generations (Ardia et al.; Mitchell, 1998; Mullen et al., 2011).

Biology-inspired optimization algorithms have been in use since the 1950s (Mitchell, 1998), also known as evolutionary algorithms (Mullen et al., 2011). However, genetic algorithms were not invented until the 1960s by John Holland, those algorithms are able of performing logical operations, crossovers, mutations, and selections on a population (Mullen et al., 2011).

Differential Evolution (DE) is a search heuristic introduced by Storn and Price (1997) and Deoptim, is the R implementation of *Differential Evolution* (DE) algorithm, was created in 2005 by David Ardia et al..

The Differential Evolution algorithm solves optimization problems by evolving a population of candidate solutions (Ardia et al.). It checks within the population (function to be evaluated), after fixing a range of evaluation, upper and lower value for each variable and the size of the sample can also be set by the user, it evaluates in that sample which of the individuals or points represents a minimum of the objective function. Next, they select that point as a floating or candidate value in which a sample will be randomly drawn around that value from the previous iteration, but this time the sample is concentrated more and more within around the previously evaluated minimum. So in package DEoptim searches for minima of the objective function between lower and upper bounds on each parameter to be optimized (Mullen et al., 2011).

DE is particularly well-suited to find the global optimum of a real-valued function of real-valued parameters, and does not require that the function be either continuous or differentiable (Mullen et al., 2011). Therefore, DE is useful in situations in which the objective function is stochastic, noisy,

or difficult to differentiate, nevertheless, may be inefficient on smooth functions, where derivative-based methods generally are most efficient (Mullen et al., 2011).

Genetic algorithms have proven to be useful heuristic methods for global optimization, in particular for combinatorial optimization problems (Ardia et al.; Mullen et al., 2011). In figure 5.16 it can see an example of an implementation of DEoptim algorithm

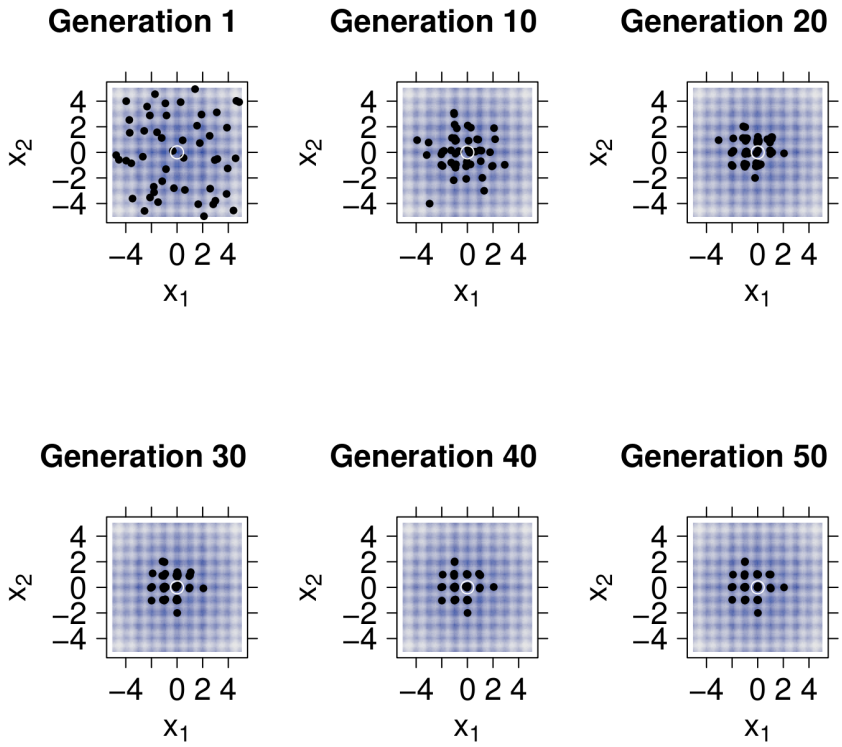

Fig. 5.16: The population associated with various generations of a call to DEoptim as it searches for the minimum of the Rastrigin function (marked with an open white circle) Mullen et al. (2011)

5.4 Final Results

At the beginning, during the simulations the algorithm of *Levenberg-Marquardt algorithm* (LMA) did not converge because the values measured in the laboratory were being used without being smoothed. Therefore, this noise made the objective function difficult to optimized by this method because there were many fluctuations in the objective function so it was tricky to get an accurate numerical approximation of it's derivatives at certain points.
Then, we though that could be an issue related with rounding error of the algorithm and for this reason it was decided to increase the precision of the values by performing the simulations and the parameterization with double and quad precision. It was also thought that the algorithm was converting local extrema, to try to solve that the objective function was multiplied to facilitate the algorithm's convergence. Since, it was not a rounding problem, this increase in the precision of the values used in the computations was not useful because it did not converge neither and increase a lot the computational time consumption of the algorithms.
This is why it was decided to use a second algorithm, the *Differential Evolution Optimization Algorithm* (DEoptim), since this second is a metaheuristic algorithm that works even with functions that are not differential. This second algorithm worked, however it was concluded that using the smoothed measurement functions observed in the laboratory, the Levenberg-Marquarat method was the fastest, it converged faster always giving the same value, while the DEoptim was slower to converge and differed by the minimum each time the algorithm was executed due to its the randomness. Figures 5.23 and 5.24 show the heat map of Objective functions for the scenarios 1 and 2 in the experiments for determine the kinematic wave of the study watershed, and the hydraulics parameters that influence in the water flux, as the Manning's roughness coefficient. According to the figures 5.23 and 5.24 it can be visualize the values where the objective function is

minimal in each scenario.

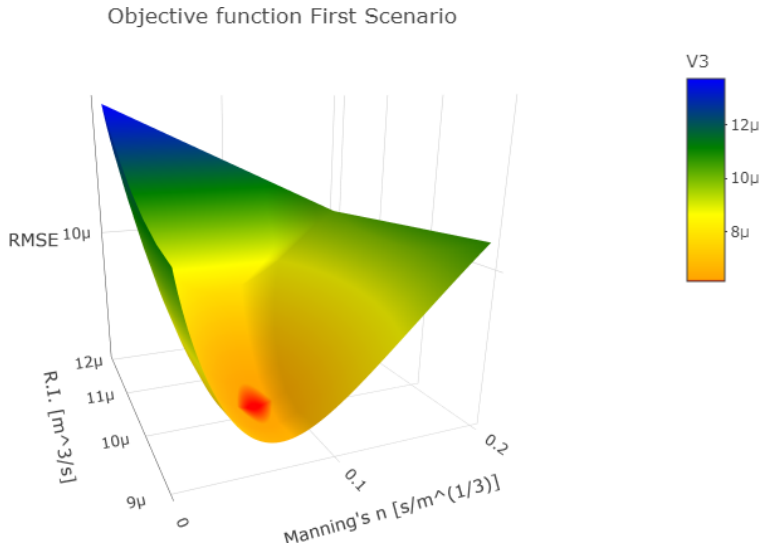

Fig. 5.17: Objective function for scenario one

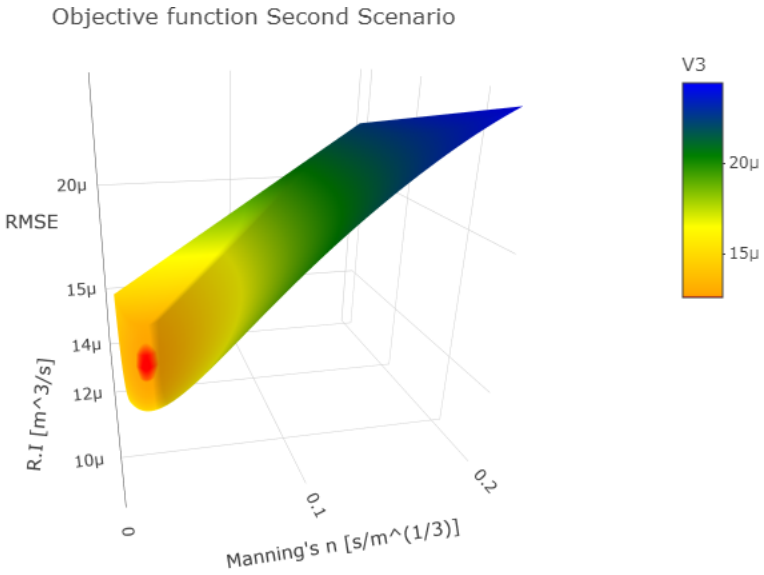

Fig. 5.18: Objective function for scenario two

In the Figure 5.19 an approximation of the minimal values can be observed, this approximation is due to the precision of the mouse position in the screen. The RMSE is minimal in the first scenario at 10 m/h, which is 36 mm of rainfall intensity and 0.0745 of Manning's roughness; the setting of this parameters brings an error value of $6.16 \cdot 10^{-9} m^3/s$. In the second scenario the minimal value of RMSE function is at 13 m/h of rainfall intensity and 0.0239, those settings values of variables are equivalent to there being an error of $12.66 \cdot 10^{-9} m^3/s$.
However, despite the fact that these data are not the most precise, it can be seen in figures 5.19 that the second scenario presents a greater approximation error. The Manning roughness behavior curve is steeper than the parabolic observed for the first scenario. This may be due to the fact that the steeper the slope of the watershed, the gravitational force is higher, then the flow and, the change in the parameters of Manning roughness and intensity of precipitation for the flow supposes a large response variance (error).

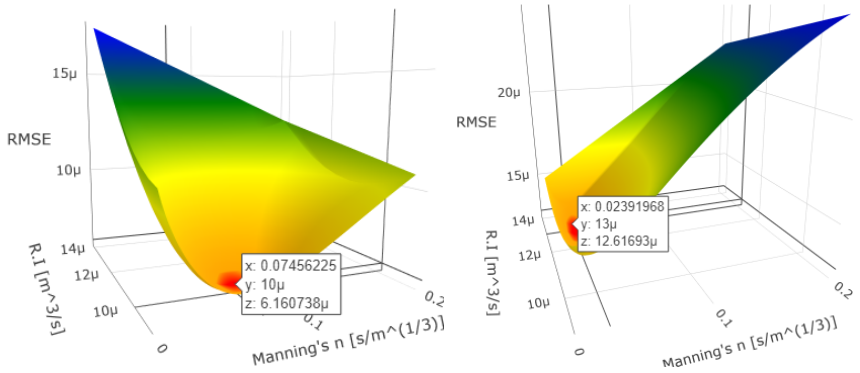

Fig. 5.19: First observation of raw data

On the other hand, it is also observed that in the first scenario with a gentler slope, the gravitational force is lower and the influence of the precipitation intensity parameter is observed higher than the second scenario where this parameter t seems "constant". The friction force due to roughness

is significant in the first scenario but lower than in the second scenario. Since these are areas where the error increases significantly. Summarizing, it can be observed that the areas where the error (RMSE) is greater, for the first scenario, where the Manning roughness coefficient is lower and the rainfall intensity is greater, just the opposite of what occurs in scenario 2.

In the following table and figure 5.20, an example of an execution of the DEoptim, the parameters are shown where the objective functions are minimized giving values that are of very low magnitude and therefore, our approximation is quite precise and accurate. In figure 5.20 it can been observed that the values of parameter are close to the parameters that appear in the table below.
Now the values at which the objective function are minimized are used to simulate the flow functions, and below is the comparison of these approximate simulated functions together with the original laboratory functions.The data used to approximate the simulation functions were:

- For scenario 1, a precipitation intensity value of $10.3^{-6} m/s$ was used, which is 37.08 mm/h and an n of 0.06 $s/m^{1/3}$.
- For scenario 2, a precipitation intensity value of $13.1^{-6} m/s$ was used, which is 47.16 mm/h and an n of 0.015 $s/m^{1/3}$.

Settings Parameters			RMSE $[m^3]$
Scenario one	N $[h/m^{1/3}]$	0.0566425702811245	9.42217368286969e-06
	R.I $[m/s]$	0.000010	
Scenario two	N $[h/m^{1/3}]$	0.0122329317269076	1.66852193434572e-05
	R.I $[m/s]$	0.000012	

Tab. 5.2: Summary of simulation results

```
upper <-c(12e-6,0.1)
lower <-c(10e-6,0.001)
itermax = 3
#NP,itermax it increases the time
y <- DEoptim.control(VTR = 0,strategy = 2, bs = FALSE, NP = 30,
                     itermax = itermax, CR = 0.75, F = 0.9, trace = TRUE,
                     initialpop = NULL, storepopfrom = itermax +1,
                     storepopfreq = 1, p = 0.2, c = 0, reltol = sqrt(.Machine$d
                     steptol = itermax)
x <- DEoptim(lower,upper, fn = rundru, control = y)

outDEoptim <- x
plot(outDEoptim)

#is slow
```

```
Console  Terminal  Jobs
C:/drutes-kinwave/eyre/
Fortran runtime error: End of file

Error termination. Backtrace:
#0  0x7f303e60d8b0 in ???
#1  0x7f303e60e395 in ???
#2  0x7f303e60eb1a in ???
#3  0x7f303e806ebb in ???
#4  0x7f303e8001b6 in ???
#5  0x7f303e8018f9 in ???
#6  0x7f303e91c423 in __postpro_MOD_get_ram_use
      at src/tools/postpro.f90:549
#7  0x7f303e8aa6b4 in MAIN__
      at src/core/main.f90:178
#8  0x7f303e8aa709 in main
      at src/core/main.f90:32
Read 1 item
Iteration: 3 bestvalit: 0.000009 bestmemit:    0.000011    0.056344
```

Fig. 5.20: Results of optimized simulation for the second scenario

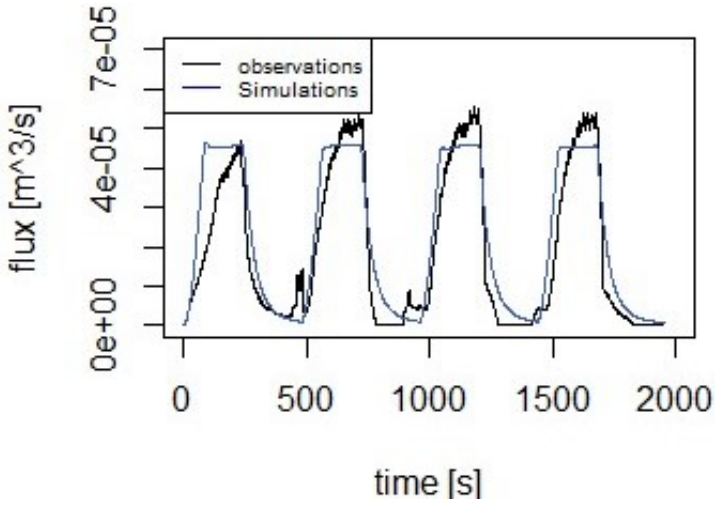

Fig. 5.21: Results of optimized simulation for the first scenario

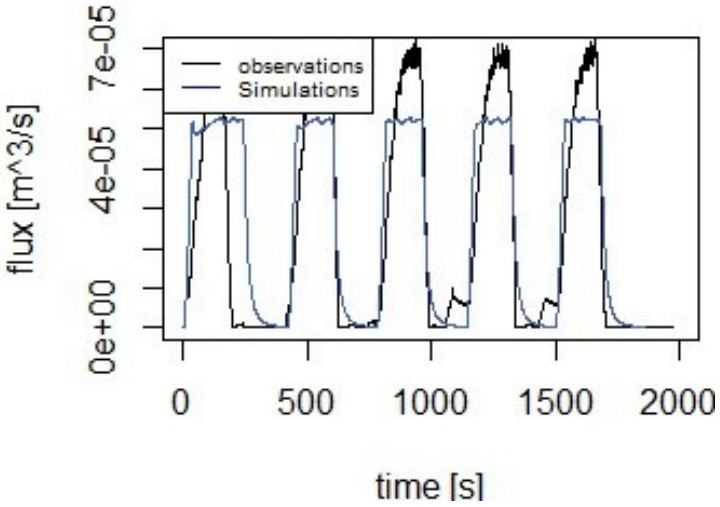

Fig. 5.22: Results of optimized simulation for the second scenario

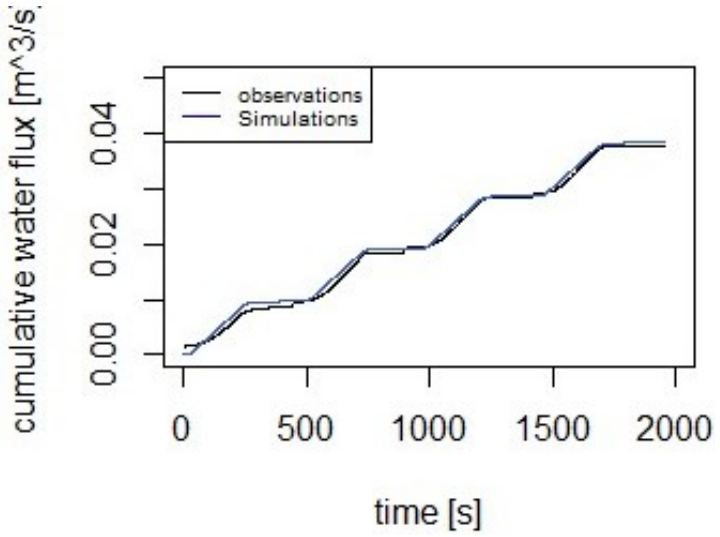

Fig. 5.23: Results of optimized simulation for the first scenario

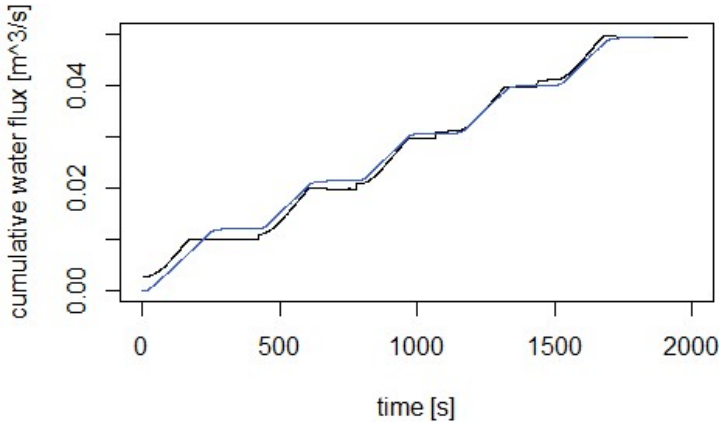

Fig. 5.24: Results of optimized simulation for the second scenario

Table 4.
Resistance parameters for overland flow

Surface	Laminar flow (k_o)	Turbulent flow	
		Manning's n	Chezy C
			$ft^{1/2}/s$
Concrete or asphalt	24 - 108	0.01 - 0.013	73 - 38
Bare sand	30 - 120	.01 - .016	65 - 33
Graveled surface	90 - 400	.012 - .03	38 - 18
Bare clay-loam soil (eroded)	100 - 500	.012 - .033	36 - 16
Sparse vegetation	1,000 - 4,000	.053 - .13	11 - 5
Short grass prairie	3,000 - 10,000	.10 - .20	6.5 - 3.6
Bluegrass sod	7,000 - 40,000	.17 - .48	4.2 - 1.8

Source: Woolhiser (1975).

Fig. 5.25: Tabulated Manning Roughness coefficient source from Woolhiser et al. (1990)

According to these results, it means that at the end of each performance a total of 64.56 L and 78.53 L for the first and second scenarios respectively were released in the rainfall simulator. There are 0.0094 L and 0.0167 L of uncertainties between the observed and simulated data, for the first and second scenarios respectively after the fitted. It can be assumed that the functions are adjusted by choosing the parameters well.

The Manning's coefficient results we find tabulated as *bare sand* and *sparce vegetation*. However, both scenarios comply with a good adjustment under the same Manning coefficient of 0.015 that corresponds to *bare sand* and *gravel surface* 5.25.

Regarding the experiment related to the transport of ash, no data analysis was finally developed, since the inconveniences at the time of optimization extended the first part of the data analysis in time.

Once the laboratory results were obtained, the data have to be reorganized with their collection time, to obtain the ash dispersion function through the study hydrographic watershed during the experimentation time (approximately half an hour). Once the database with the ash concentrations had been reorganized, an inverse analysis model had to be performance again.

CHAPTER 6

Conclusion

This project is presented as a study of a laboratory experiment developed to investigated the ash flow equation. A model was used for the assessment of risk of water quality in water supply catchments after a wildfire event. The model mainly determine the advective component of the flow with a kinematic wave approximation and how it influences the transport of the pollutant. The hydraulic parameters that we are interested on include the variables rainfall intensity, slope and Manning's roughness coefficient. An inverse model was developed, comparing the results observed in the laboratory with the results simulated by DRUtES software. To fit the simulated results with the observed ones some iterative algorithms like LMA and DEoptim were used to find the right values of those paremeters that minimized the objective function. We had to deal with problems of data uncertainty and non-derivable functions (that exhibit peaks and strong variation) and therefore, with problems with the convergence of the algorithms.

In conclusion, the concern about the threat of fire in drinking water supply is already at the scientific and political level. This project shows that the

determination of the ash flow in laboratory under certain conditions can guide the water supply managers towards a more effective response. These results may be applied to find the vulnerable areas, with topographic slopes and climatology conditions prone to ash contamination after a fire. Maybe the same experiment could be developed with different soil substratum in order to determine different friction behaviours. The importance of water treatments and the chemical and physical characteristics of the ashes (Bodí et al., 2012; Santín et al., 2015) continue to be investigated. Beyond the chemical pollutant effects when ash reaches the reservoir, there is a physical effect (turbidity) due to the suspended solids (Santín et al., 2015). Finally, an adequate updating management, policies and procedures of forest masses are necessary to try to prevent fires. Dry fuel must be eliminated and therefore the suppression of felling is not beneficial.

Bibliography

Hafzullah Aksoy, N Erdem Unal, Sevket Cokgor, Abdullah Gedikli, Jaeyoung Yoon, Kaan Koca, S Boran Inci, and Ebru Eris. A rainfall simulator for laboratory-scale assessment of rainfall-runoff-sediment transport processes over a two-dimensional flume. *Catena*, 98:63–72, 2012.

David Ardia, Katharine M Mullen, Brian G Peterson, and Joshua Ulrich. Deoptim: Differential evolution in r. 2016. *URL https://CRAN. R-project. org/package= DEoptim*.

Ralph Alger Bagnold. *An approach to the sediment transport problem from general physics*. US government printing office, 1966.

Jamie Bartram, Niels Thyssen, and Alison Gowers. *Water and health in Europe: a joint report from the European Environment Agency and the WHO Regional Office for Europe*. Number 93. WHO Regional Office Europe, 2002.

Keith J Beven. Rainfall-runoff modelling: The primer 2d edition isbn: 978-0-470-71459-1 488 pages february 2012, 2012.

Merche B Bodí, Jorge Mataix-Solera, Stefan H Doerr, and Artemi Cerdà. The wettability of ash from burned vegetation and its relationship to mediterranean plant species type, burn severity and total organic carbon content. *Geoderma*, 160(3-4):599–607, 2011.

Merche B Bodí, Stefan H Doerr, Artemi Cerdà, and Jorge Mataix-Solera. Hydrological effects of a layer of vegetation ash on underlying wettable and water repellent soil. *Geoderma*, 191:14–23, 2012.

John Alexander Henstridge Brown. Hydrologic effects of a bushfire in a catchment in south-eastern new south wales. *Journal of Hydrology*, 15 (1):77–96, 1972.

A.R. Buda. 7.7 surface-runoff generation and forms of overland flow. In John F. Shroder, editor, *Treatise on Geomorphology*, pages 73–84. Academic Press, San Diego, 2013. ISBN 978-0-08-088522-3. doi: https://doi.org/10.1016/B978-0-12-374739-6.00151-2. URL `https://www.sciencedirect.com/science/article/pii/B9780123747396001512`.

Federica Cappelli, Caterina Conigliani, Davide Consoli, Valeria Costantini, and Elena Paglialunga. Climate change and armed conflicts in africa: temporal persistence, non-linear climate impact and geographical spillovers. *Economia Politica*, pages 1–44, 2022.

A Cerdà. Changes in overland flow and infiltration after a rangeland fire in a mediterranean scrubland. *Hydrological processes*, 12(7):1031–1042, 1998.

E Ward Cheney and David R Kincaid. *Numerical mathematics and computing*. Cengage Learning, 2012.

Ven Te Chow, David R Maidment, and Larry W Mays. *Hidrología aplicada*. McGraw-Hill, 1996.

Michelle A Clarke and Rory PD Walsh. A portable rainfall simulator for field assessment of splash and slopewash in remote locations. *Earth Surface Processes and Landforms: The Journal of the British Geomorphological Research Group*, 32(13):2052–2069, 2007.

Ryan P Cole, Kevin D Bladon, Joseph W Wagenbrenner, and Drew BR Coe. Hillslope sediment production after wildfire and post-fire forest management in northern california. *Hydrological Processes*, 34(26):5242–5259, 2020.

Leonard F DeBano. The role of fire and soil heating on water repellency in wildland environments: a review. *Journal of hydrology*, 231:195–206, 2000.

Leonard F DeBano, Raymond M Rice, and Conrad C Eugene. Soil heating in chaparral fires: effects on soil properties, plant nutrients, erosion, and runoff. *Res. Paper PSW-RP-145. Berkeley, CA: US Department of Agriculture, Forest Service, Pacific Southwest Forest and Range Experiment Station. 21 p*, 145, 1979.

Randall J Donohue, TIM R McVICAR, and Michael L Roderick. Climate-related trends in australian vegetation cover as inferred from satellite observations, 1981–2006. *Global Change Biology*, 15(4):1025–1039, 2009.

Nigel Dudley and Sue Stolton. *Running pure: the importance of forest protected areas to drinking water*. World Bank/WWF Alliance for Forest Conservation and Sustainable Use, 2003.

Brian A Ebel, John A Moody, and Deborah A Martin. Hydrologic conditions controlling runoff generation immediately after wildfire. *Water Resources Research*, 48(3), 2012.

Emmanuel J Gabet. Post-fire thin debris flows: sediment transport and numerical modelling. *Earth Surface Processes and Landforms: The Journal of the British Geomorphological Research Group*, 28(12):1341–1348, 2003.

Tai-Ran Hsu. *Applied engineering analysis*. John Wiley & Sons, 2018.

San-Miguel-Ayanz J, Durrant T, Boca R, Maianti P, Liberta' G, Artes Vivancos T, Jacome Felix Oom D, Branco A, De Rigo D, Ferrari D, Pfeiffer H, Grecchi R, Onida M, and Loffler P. Forest fires in europe, middle east and north africa 2021. (KJ-NA-31-269-EN-N (online),KJ-NA-31-269-EN-C (print)), 2022. ISSN 1831-9424 (online),1018-5593 (print). doi: 10.2760/34094(online),10.2760/058256(print).

Dennis L Johnson and Arthur C Miller. A spatially distributed hydrologic model utilizing raster data structures. *Computers & Geosciences*, 23(3): 267–272, 1997.

P Kavka, M Neumann, T Laburda, and D Zumr. Developing of the laboratory rainfall simulator for testing the technical soil surface protection measures and droplets impact. In *Proceedings of the XVII ECSMGE-2019 European Conference on Soil Mechanics and Geotechnical Engineering, Reykjavik, Iceland*, pages 1–6, 2019.

JG Kroes, JC Van Dam, RP Bartholomeus, P Groenendijk, M Heinen, RFA Hendriks, HM Mulder, I Supit, and PEV Van Walsum. Swap version 4. Technical report, Wageningen Environmental Research, 2017.

Michal Kuráž and Petr Mayer. Algorithms for solving darcian flow in structured porous media. *Acta Polytechnica*, 53(4), 2013.

Patrick NJ Lane, Gary J Sheridan, and Philip J Noske. Changes in sediment loads and discharge from small mountain catchments following wildfire in south eastern australia. *Journal of Hydrology*, 331(3-4):495–510, 2006.

Christoph Langhans, Hugh G Smith, Derek MO Chong, Petter Nyman, Patrick NJ Lane, and Gary J Sheridan. A model for assessing water quality risk in catchments prone to wildfire. *Journal of Hydrology*, 534: 407–426, 2016.

Kenneth Levenberg. A method for the solution of certain non-linear problems in least squares. *Quarterly of applied mathematics*, 2(2):164–168, 1944.

James A Liggett and David A Woolhiser. The use of the shallow water equations in runoff computation. In *Proc. 3rd annual amer. water resources conf*, pages 117–126, 1967.

Xin Liu. A robust numerical model for shallow water governing solute transport with wet/dry interfaces. *Computer Methods in Applied Mechanics and Engineering*, 351:85–108, 2019.

James J McCarthy, Osvaldo F Canziani, Neil A Leary, David J Dokken, Kasey S White, et al. *Climate change 2001: impacts, adaptation, and vulnerability: contribution of Working Group II to the third assessment report of the Intergovernmental Panel on Climate Change*, volume 2. Cambridge University Press, 2001.

Jeffrey E Miller. Basic concepts of kinematic-wave models. Technical report, US Geological Survey, 1984.

Melanie Mitchell. *An introduction to genetic algorithms*. MIT press, 1998.

John A Moody and Deborah A Martin. Post-fire, rainfall intensity–peak discharge relations for three mountainous watersheds in the western usa. *Hydrological processes*, 15(15):2981–2993, 2001.

John A Moody, Deborah A Martin, Sandra L Haire, and David A Kinner. Linking runoff response to burn severity after a wildfire. *Hydrological Processes: An International Journal*, 22(13):2063–2074, 2008.

EM Morris and David A Woolhiser. Unsteady one-dimensional flow over a plane: Partial equilibrium and recession hydrographs. *Water Resources Research*, 16(2):355–360, 1980.

Chantal Mouël and Agneta Forslund. How can we feed the world in 2050? a review of the responses from global scenario studies. *European Review of Agricultural Economics*, 44, 09 2017. doi: 10.1093/erae/jbx006.

Katharine Mullen, David Ardia, David L Gil, Donald Windover, and James Cline. Deoptim: An r package for global optimization by differential evolution. *Journal of Statistical Software*, 40(6):1–26, 2011.

Gerald C Nelson, Mark W Rosegrant, Amanda Palazzo, Ian Gray, Christina Ingersoll, Richard Robertson, Simla Tokgoz, Tingju Zhu, Timothy B Sulser, Claudia Ringler, et al. *Food security, farming, and climate change to 2050: scenarios, results, policy options*, volume 172. Intl Food Policy Res Inst, 2010.

Viviane Philipps, Boris P Hejblum, Mélanie Prague, Daniel Commenges, and Cécile Proust-Lima. Robust and efficient optimization using a marquardt-levenberg algorithm with r package marqlevalg. *arXiv preprint arXiv:2009.03840*, 2020.

Hans-O Pörtner, Debra C Roberts, Helen Adams, Carolina Adler, Paulina Aldunce, Elham Ali, Rawshan Ara Begum, Richard Betts, Rachel Bezner Kerr, Robbert Biesbroek, et al. *Climate change 2022: Impacts, adaptation and vulnerability*. IPCC Geneva, Switzerland:, 2022.

Jose Pujol. The solution of nonlinear inverse problems and the levenberg-marquardt method. *Geophysics*, 72(4):W1–W16, 2007.

Ananth Ranganathan. The levenberg-marquardt algorithm. *Tutoral on LM algorithm*, 11(1):101–110, 2004.

Steven L Reneau, Danny Katzman, Gregory A Kuyumjian, Alexis Lavine, and Daniel V Malmon. Sediment delivery after a wildfire. *Geology*, 35 (2):151–154, 2007.

Brian D Ripley et al. The r project in statistical computing. *MSOR Connections. The newsletter of the LTSN Maths, Stats & OR Network*, 1 (1):23–25, 2001.

Sandra E Ryan, Kathleen A Dwire, and Mark K Dixon. Impacts of wildfire on runoff and sediment loads at little granite creek, western wyoming. *Geomorphology*, 129(1-2):113–130, 2011.

Cristina Santín, Stefan H Doerr, Xosé L Otero, and Chris J Chafer. Quantity, composition and water contamination potential of ash produced under different wildfire severities. *Environmental Research*, 142:297–308, 2015.

DJ Semmens, DC Goodrich, CL Unkrich, RE Smith, DA Woolhiser, SN Miller, et al. Kineros2 and the agwa modelling framework. *Hydrological modelling in arid and semi-arid areas*, page 49, 2007.

Richard A Shakesby and Stefan H Doerr. Wildfire as a hydrological and geomorphological agent. *Earth-Science Reviews*, 74(3-4):269–307, 2006.

Priyadarshi R Shukla, J Skea, R Slade, R van Diemen, E Haughey, J Malley, M Pathak, J Portugal Pereira, F Agus, A Arneth, et al. Technical summary. 2019.

Jirka Simunek, M Th Van Genuchten, and M Sejna. The hydrus-1d software package for simulating the one-dimensional movement of water, heat, and multiple solutes in variably-saturated media. *University of California-Riverside Research Reports*, 3:1–240, 2005.

Hugh G Smith, Gary J Sheridan, Patrick NJ Lane, Petter Nyman, and Shane Haydon. Wildfire effects on water quality in forest catchments: A review with implications for water supply. *Journal of Hydrology*, 396 (1-2):170–192, 2011.

Filip Stanić, Nenad Jaćimović, Anja Ranđelović, and Jovan Despotović. Laboratory investigation of hydraulic characteristics of fly ash as a fill material from the aspects of pollutant transport. *Water Science and Technology*, 76(4):976–982, 2017.

UNICEF et al. State of the world's drinking water. 2022.

Jos C Van Dam and Reinder A Feddes. Numerical simulation of infiltration, evaporation and shallow groundwater levels with the richards equation. *Journal of Hydrology*, 233(1-4):72–85, 2000.

Ian White, Alan Wade, Martin Worthy, Norm Mueller, Trevor Daniell, and Robert Wasson. The vulnerability of water supply catchments to bushfires: impacts of the january 2003 wildfires on the australian capital territory. *Australasian Journal of Water Resources*, 10(2):179–194, 2006.

Richard J Williams, Anthony D Griffiths, Grant E Allan, et al. Fire regimes and biodiversity in the savannas of northern australia. *Flammable Australia: the fire regimes and biodiversity of a continent*, pages 281–304, 2002.

Peter Wilson and H Alan Mantooth. *Model-based engineering for complex electronic systems*. Newnes, 2013.

David A Woolhiser, Roger E Smith, Dana C Goodrich, et al. Kineros: a kinematic runoff and erosion model: documentation and user manual. 1990.

David Arthur Woolhiser and James A Liggett. Unsteady, one-dimensional flow over a plane—the rising hydrograph. *Water Resources Research*, 3 (3):753–771, 1967.